

# Distinct descending motor cortex pathways and their roles in movement

Michael N. Economo<sup>1</sup>, Sarada Viswanathan<sup>1</sup>, Bosiljka Tasic<sup>2</sup>, Erhan Bas<sup>1</sup>, Johan Winnubst<sup>1</sup>, Vilas Menon<sup>1</sup>, Lucas T. Graybuck<sup>2</sup>, Thuc Nghi Nguyen<sup>2</sup>, Kimberly A. Smith<sup>2</sup>, Zizhen Yao<sup>2</sup>, Lihua Wang<sup>1</sup>, Charles R. Gerfen<sup>3</sup>, Jayaram Chandrashekar<sup>1</sup>, Hongkui Zeng<sup>2</sup>, Loren L. Looger<sup>1</sup> & Karel Svoboda<sup>1\*</sup>

**Activity in the motor cortex predicts movements, seconds before they are initiated. This preparatory activity has been observed across cortical layers, including in descending pyramidal tract neurons in layer 5. A key question is how preparatory activity is maintained without causing movement, and is ultimately converted to a motor command to trigger appropriate movements. Here, using single-cell transcriptional profiling and axonal reconstructions, we identify two types of pyramidal tract neuron. Both types project to several targets in the basal ganglia and brainstem. One type projects to thalamic regions that connect back to motor cortex; populations of these neurons produced early preparatory activity that persisted until the movement was initiated. The second type projects to motor centres in the medulla and mainly produced late preparatory activity and motor commands. These results indicate that two types of motor cortex output neurons have specialized roles in motor control.**

Motor cortex activity anticipates specific future movements, often seconds before the onset of movement<sup>1,2</sup>. This dynamic process, referred to as preparatory activity, moves motor cortex population activity to an initial condition that is appropriate for eliciting rapid, accurate movements<sup>2</sup>. In addition, motor cortex activity is modulated milliseconds before and during the onset of movement, consistent with commands that control the timing and direction of movements<sup>3,4</sup>.

Reconciling these dual roles of the motor cortex requires an understanding of motor cortex cell types, and how these cell types integrate into multi-regional circuits. The motor cortex comprises cell types that differ in their location, gene expression, electrophysiology and connectivity. Intratelencephalic neurons in layers (L) 2–6 receive input from other cortical areas and excite pyramidal tract (PT) neurons<sup>5–7</sup>. PT neurons, the somata of which define neocortical L5b<sup>8</sup>, link the motor cortex with premotor centres in the brainstem and spinal cord<sup>9,10</sup> and directly influence behaviour<sup>10–12</sup>. PT neurons also project to the thalamus<sup>6,13,14</sup>. Preparatory activity requires reverberations in a thalamocortical loop<sup>15</sup>. Consistent with roles in both the planning and initiation of movement, PT neurons are structurally heterogeneous<sup>14,16,17</sup> and show diverse activity patterns, including preparatory activity and movement commands<sup>18–20</sup>.

Here we show that PT neurons in the mouse motor cortex comprise two cell types with distinct gene expression and axonal projections. We refer to these cell types as PT<sub>upper</sub> and PT<sub>lower</sub> neurons, reflecting their distributions in different sublaminae in L5b. PT<sub>upper</sub> neurons project to the thalamus, which forms a feedback loop with the motor cortex. PT<sub>lower</sub> cells project to premotor centres in the medulla. Cell-type-specific extracellular recordings in the anterior lateral motor cortex (ALM) during a delayed-response task suggest that PT<sub>upper</sub> neurons are preferentially involved in motor planning, whereas PT<sub>lower</sub> neurons have roles in movement execution.

## Two types of PT neuron in layer 5

Single-cell RNA sequencing (scRNA-seq) was used to produce a taxonomy of cell types in the ALM and visual cortex<sup>21</sup>. From 9,573 single-cell

transcriptomes, glutamatergic neurons in the ALM were grouped into 27 clusters (Fig. 1), which were distinct from glutamatergic clusters identified in the visual cortex<sup>21</sup>. PT neurons form the sole cortical projection to motor areas in the midbrain and hindbrain, and are therefore likely to have important roles in motor planning and execution. ALM PT neurons mapped to three transcriptomic clusters: the *Slco2a1* cluster and two other closely related clusters (*Npsr1* and *Hpgd*; Fig. 1 and Extended Data Fig. 1).

We mapped the structural diversity of PT neurons by reconstructing individual cells<sup>22</sup> ( $n = 12$ ; Fig. 2a, b and Supplementary Table 1; median axonal length: 121,037  $\mu\text{m}$ , range: 80,873–188,105  $\mu\text{m}$ ; median branch points: 243, range: 144–540). Patterns of axonal collaterals revealed two neuron types: one group innervated the thalamus ( $n = 8$ ; Fig. 2a, b; green hues and Extended Data Fig. 2); the other group bypassed the thalamus and branched in the medulla, including the reticular nuclei containing premotor neurons for orofacial movements<sup>23</sup> ( $n = 4$ ; magenta hues). All cells innervated the superior colliculus and subsets of both groups branched in other areas (Fig. 2a, b and Extended Data Fig. 2).

We used the adeno-associated virus rAAV2-retro<sup>24</sup> to label neurons retrogradely from the thalamus and medulla. Thalamus-projecting PT neurons were in upper L5b (Fig. 2c, d and Extended Data Fig. 3; green cells)<sup>6</sup> and medulla-projecting PT neurons were in lower L5b (magenta cells). This pattern was similar across the primary and secondary motor cortex (Extended Data Fig. 3). Retrograde labelling from the superior colliculus and pons labelled PT neurons in both L5b sublaminae (Fig. 2c). Few neurons were co-labelled by injections into the thalamus and medulla (2.2%; 22 out of 984 cells labelled from either location), whereas many neurons were co-labelled by injections into the thalamus and superior colliculus (77.1%; 687 out of 890 thalamus-labelled cells), as expected from axonal reconstructions.

To link projection classes and transcriptomic clusters, we examined gene expression in medulla-projecting and thalamus-projecting PT neurons identified using rAAV2-retro. All (62 out of 62) medulla-projecting PT neurons mapped to the *Slco2a1* taxonomic cluster.

<sup>1</sup>Janelia Research Campus, Howard Hughes Medical Institute, Ashburn, VA, USA. <sup>2</sup>Allen Institute for Brain Science, Seattle, WA, USA. <sup>3</sup>National Institute of Mental Health, Bethesda, MD, USA.  
\*e-mail: svobodak@janelia.hhmi.org

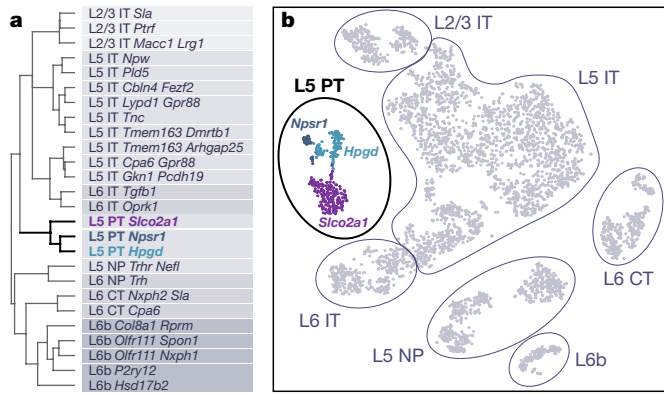


**Fig. 1 | Taxonomy of motor cortex glutamatergic neurons based on scRNA-seq.** **a**, Hierarchical clustering based on gene expression (for details, see Tasic et al.<sup>21</sup>). Three transcriptomic clusters, identified by the genes *Slco2a1*, *Npsr1* and *Hpgd*, correspond to PT neurons. The transcriptomic cluster corresponding to Cajal–Retzius cells was excluded here<sup>21</sup>. CT, corticothalamic neurons; IT, intratelencephalic neurons; NP, near-projecting neurons. *Ptf1* is also known as *Cavin1*. **b**, Two-dimensional stochastic neighbour embedding (*t*-SNE) of transcriptomic data of sequenced single neurons in the ALM ( $n = 4,477$  glutamatergic cells). Cells are colour-coded as in **a**.

Similarly, thalamus-projecting PT neurons mapped to the *Npsr1* and *Hpgd* clusters (91 out of 94, *Npsr1*: 19 out of 94, *Hpgd*: 72 out of 94; Figs. 1b, 2e, f). Pons- and superior colliculus-projecting neurons mapped to the same three PT clusters (superior colliculus total: 97, *Slco2a1*: 43, *Npsr1*: 15, *Hpgd*: 39; pons total: 100, *Slco2a1*: 86, *Npsr1*: 5, *Hpgd*: 9; Fig. 2f). Expression patterns of neurons in the *Slco2a1* cluster retrogradely labelled from a single structure (that is, superior colliculus, pons or medulla) were not more similar to each other than in pairs drawn randomly from the *Slco2a1* cluster (Extended Data Fig. 4a). Likewise, the projection targets of *Hpgd* neurons (that is, superior colliculus or thalamus) did not explain additional gene expression variance within that cluster (Extended Data Fig. 4b, c; the *Npsr1* cluster was not analysed owing to its small size).

Axonal reconstructions and scRNA-seq data suggest that PT neurons can be divided into two distinct cell types. To determine whether thalamus-projecting and medulla-projecting PT neurons account for most PT neurons, we examined additional PT neurons that were reconstructed partially (thalamus-projecting:  $n = 3$ ; medulla-projecting:  $n = 3$ ). All (18 out of 18) partially and fully reconstructed PT neurons projected to the superior colliculus and no (0 out of 18) PT neurons lacked projections to both the thalamus and medulla (Supplementary Table 1). Thalamus- and medulla-projecting neurons together expressed the complete set of PT neuron genes (Extended Data Fig. 4d). These results suggest that most, if not all, PT neurons are accounted for by the medulla-projecting and thalamus-projecting types. We refer to the superficial, thalamus-projecting *Npsr1*–*Hpgd* cell type as PT<sub>upper</sub> neurons, and the deep, medulla-projecting *Slco2a1* cell type as PT<sub>lower</sub> neurons, reflecting their laminar distributions.

We next identified marker genes for PT<sub>upper</sub> (*Npsr1*–*Hpgd* clusters) and PT<sub>lower</sub> (*Slco2a1* cluster) neurons. For maximal sensitivity, we combined scRNA-seq with bulk RNA sequencing (RNA-seq) analysis (Extended Data Fig. 4e–i; 50–100 cells per sample; 6 replicates each). The relative expression levels of differentially expressed genes in scRNA-seq and bulk RNA-seq were highly correlated (Extended Data Fig. 4i). Differentially expressed genes identified from scRNA-seq were differentially expressed in bulk RNA-seq (Extended Data Fig. 1c), and vice versa (Extended Data Fig. 1b). Several differentially expressed genes were specific for each population. From these, *Slco2a1* was confirmed as a marker for PT<sub>lower</sub> neurons (Fig. 3). Single-molecule RNA fluorescence *in situ* hybridization (smFISH) revealed higher levels of *Slco2a1* mRNA in PT<sub>lower</sub> neurons than in PT<sub>upper</sub> neurons (Fig. 3c; bottom). *Npnt* was specific for, and spanned, both clusters containing PT<sub>upper</sub> neurons (*Npsr1* and *Hpgd*; Fig. 3a). smFISH confirmed that

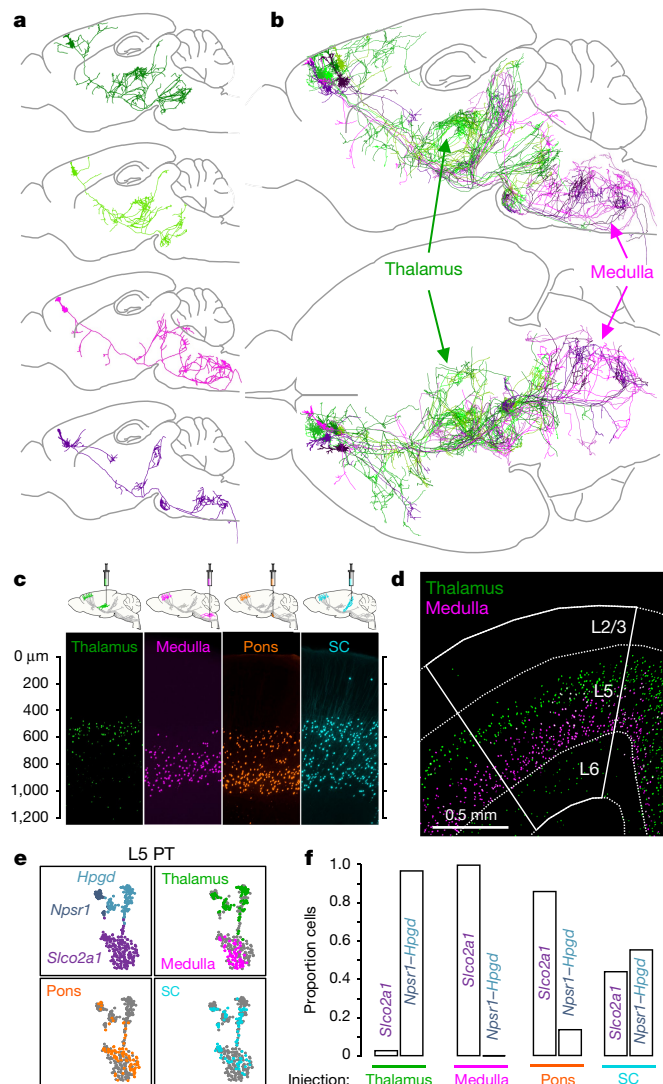


**Fig. 2 | Two types of PT neuron in the motor cortex.** **a**, Example reconstructions. Two PT neurons project to the thalamus (top; green hues) and two project to the medulla (bottom; magenta hues). **b**, Four thalamus-projecting and four medulla-projecting PT neurons overlaid and collapsed in the sagittal (top) and horizontal (bottom) planes. Dendrites are denoted by thicker lines. **c**, **d**, Nuclei of neurons retrogradely labelled from the thalamus (green) and medulla (magenta) are located in distinct sublaminae of L5b (experiment replicated three times with similar results). SC, superior colliculus. **e**, Gene expression of PT neurons coloured according to cluster membership or retrograde injection site in *t*-SNE space (as in Fig. 1b;  $n = 368$  PT neurons). **f**, Proportion of neurons retrogradely labelled from each PT target that were clustered into the *Slco2a1* and *Npsr1*–*Hpgd* expression clusters.

*Npnt* was expressed specifically in PT<sub>upper</sub> neurons (Fig. 3c; top) compared to PT<sub>lower</sub> neurons. *Npnt* and *Slco2a1* also marked PT<sub>upper</sub> and PT<sub>lower</sub> neurons in the primary motor cortex (data not shown), indicating that the gene expression patterns determined in the ALM generalize across the motor cortex.

### Cell-type-specific recordings

The projection patterns of PT<sub>upper</sub> and PT<sub>lower</sub> neurons suggest distinct roles in motor control. The cortico–thalamocortical loop is necessary for maintaining persistent preparatory activity related to motor planning<sup>15</sup>. PT<sub>upper</sub> cells project to the thalamus and lack projections to premotor nuclei in the medulla (Fig. 2a, b and Extended Data Fig. 2). These characteristics suggest a role for PT<sub>upper</sub> cells in generating and/or maintaining preparatory activity. By contrast, PT<sub>lower</sub> cells project to

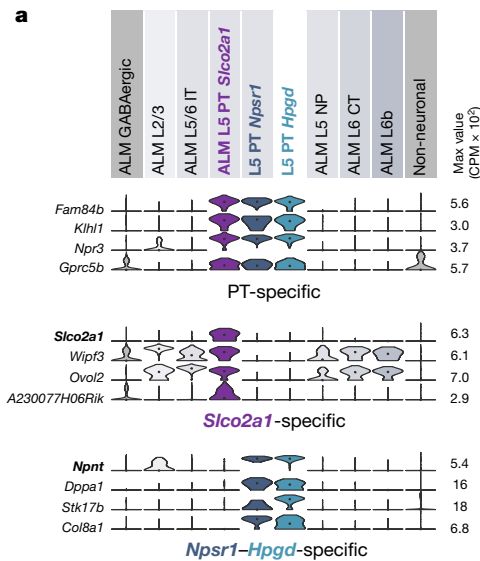


**Fig. 3 | PT neuron type markers.** **a**, Differentially expressed genes from scRNA-seq ( $n = 9,573$  cells), represented by violin plots. Each row represents a single gene, and values within rows are normalized between 0 and the maximum expression value for each gene (right) and displayed on a  $\log_{10}$  scale. Median values are shown as black dots within each violin. CPM, counts per million mapped reads. **b**, smFISH validating cell-type-specific marker expression. Blue, neurons labelled from the thalamus or

medulla; yellow, RNA puncta; grey, cellular nuclei. **c**, Number of *Npnt* (top) and *Slco2a1* (bottom) RNA puncta in the ALM measured in cells of each type. *Slco2a1*,  $PT_{upper}$ : IQR = 1–2.5 puncta,  $n = 60$ ; *Slco2a1*,  $PT_{lower}$ : IQR = 6–22,  $n = 95$ ; *Npnt*,  $PT_{upper}$ : IQR = 16–40,  $n = 145$ ; *Npnt*,  $PT_{lower}$ : IQR = 1–9,  $n = 69$ . Horizontal bars in box plots correspond to quartiles. Two independent biological replicates of the experiment illustrated in **b** and **c** yielded similar results and were pooled.

premotor centres in the medulla and spinal cord, with few collaterals in the basal ganglia and thalamus, suggesting a role in movement execution. We performed projection-specific recordings in the ALM during a delayed-response task<sup>19,25</sup> (Fig. 4). Mice were trained to discriminate object locations with their whiskers<sup>25</sup> and signal their decision about object location with skilled, directional licking (left or right) after a delay epoch (1.3 s). The delay epoch was terminated by an auditory ‘go’ cue that instructs animals to respond. The ALM is a hub for planning and executing movements in this task<sup>18,25–27</sup>.

$PT_{upper}$  or  $PT_{lower}$  cells were infected with rAAV2-retro expressing channelrhodopsin-2 (ChR2). Fibre optic cannulae were implanted into the thalamus (to activate  $PT_{upper}$  cells; Fig. 4c, top) or medulla (to activate  $PT_{lower}$  cells; Fig. 4c, bottom). ChR2-expressing cells in the ALM were identified with axonal photostimulation and extracellular recordings in the ALM using a collision test<sup>18</sup> (61  $PT_{upper}$  cells, 8 mice; 69  $PT_{lower}$  neurons, 4 mice; Fig. 4d and Extended Data Fig. 5). Identified  $PT_{upper}$  cells were at more superficial recording depths than  $PT_{lower}$  neurons, consistent with retrograde labelling experiments (Figs. 2c, d, 4e). Layer 6 corticothalamic cells, which also innervate the thalamus, were inefficiently labelled by rAAV2-retro<sup>24</sup> and excluded based on recording depth, several hundred micrometres below the  $PT_{upper}$  cells. Baseline and trial-averaged peak spike rates were not significantly different ( $P > 0.1$ , two-sided  $t$ -test) in  $PT_{upper}$  cells (baseline:  $4.3 \pm 3.5$  Hz; peak:  $17.7 \pm 13.8$  Hz; median  $\pm$  s.d.) compared to  $PT_{lower}$  cells (baseline:  $5.2 \pm 4.8$  Hz; peak:  $17.2 \pm 22$  Hz). Spike rates in  $PT_{lower}$  cells were more heterogeneous across the population (baseline:  $P = 0.02$ ; peak:  $P = 3 \times 10^{-4}$ ;  $\chi^2$  test). A substantial proportion of  $PT_{lower}$  neurons displayed spike bursts (18.8%), which were rare among  $PT_{upper}$  cells (3.3%;  $P = 0.006$ , Fisher’s exact test; Extended Data Fig. 5c).

Most recorded PT neurons had significant selectivity, defined as the difference in spike rate between trial types (‘lick left’ versus ‘lick right’), during at least one task epoch ( $P < 0.01$ , two-sided Mann–Whitney  $U$ -test; 122 out of 130; 94%). Individual neurons exhibited diverse patterns of activity and selectivity (Fig. 4f and Extended Data Fig. 5). Trial-averaged activity patterns were nearly as diverse within each PT population as across all neurons recorded within ALM (Extended Data Fig. 6). We next investigated how specific task-related signals were represented in each PT population.

## Preparatory activity

A subset of PT neurons displayed selectivity that emerged at the start of the sample epoch and persisted through the delay epoch (Fig. 4f; left cells), representing a stable encoding of upcoming movement direction<sup>1</sup>.

We investigated the emergence and maintenance of preparatory activity in populations of  $PT_{upper}$  and  $PT_{lower}$  cells. Neurons were pooled across experiments and analysed in activity space, in which each dimension corresponds to the activity of one neuron<sup>27,28</sup>. Preparatory activity for each movement corresponded to a distinct trajectory in activity space. For each population, we computed the direction in activity space that best discriminated trial types during the first 400 ms of the sample epoch (CD<sub>early</sub>: ‘early coding direction’). We then projected the trial-averaged activity of all cells in the population along CD<sub>early</sub>, producing the one-dimensional projection of each activity space trajectory with maximal selectivity (Fig. 5a). In this projection, selectivity was larger and more consistent across trials in the  $PT_{upper}$  population compared to the  $PT_{lower}$  population (Fig. 5b). Furthermore, selectivity in the  $PT_{upper}$  population remained constant throughout the sample and delay epochs until the go cue, implying retention of decision-related information. By contrast, selectivity in the  $PT_{lower}$  population decayed rapidly along CD<sub>early</sub> (no significant selectivity in 400 ms preceding go cue;  $P = 0.34$ , bootstrap). This decay did not reflect a lack of selectivity in the  $PT_{lower}$  population: along a different direction in activity space, which maximized selectivity at the end of the delay epoch, CD<sub>late</sub>, selectivity was substantial in both cell types<sup>18</sup> (Extended Data Fig. 7a, b;  $PT_{upper}$ : 40 out of 61 neurons selective;  $PT_{lower}$ : 44 out of 69). We next computed the stability of the coding direction. For the  $PT_{upper}$  population, the CD remained more similar across the sample and delay epochs compared to the  $PT_{lower}$  population (Extended Data Fig. 7c, d). Differences in coding between  $PT_{upper}$  and  $PT_{lower}$  neurons could not be explained by variation across animal cohorts (Extended Data Fig. 8). As suggested by population analyses, individual  $PT_{upper}$  neurons displayed persistent selectivity throughout the sample and delay epochs (Fig. 5c), exhibited higher early selectivity ( $PT_{upper}$ :  $0.41 \pm 0.04$ ; mean  $\pm$  s.e.m.;  $PT_{lower}$ :  $0.25 \pm 0.02$ ;  $P < 0.01$ ), and decoded trial type significantly better than  $PT_{lower}$  neurons during the sample epoch (Extended Data Fig. 9).

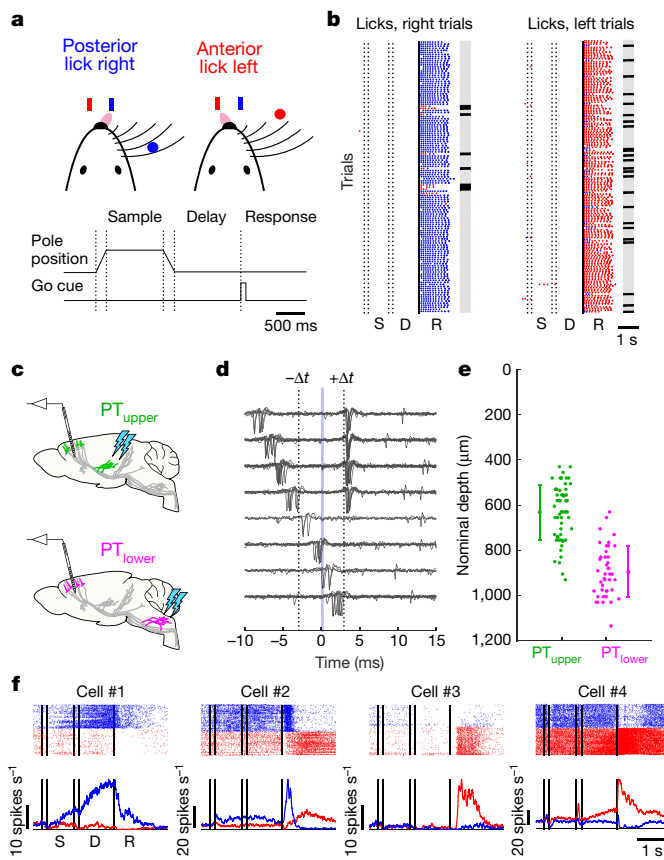


**Fig. 4 | Cell type-specific extracellular neurophysiology.** **a**, Delayed-response task. On each trial, an object was presented to the whiskers in one of two rostro-caudal positions during the sample epoch (1.0 s). After a brief delay epoch (1.3 s), mice reported the pole position by licking a reward port on the right (caudal pole position) or the left (rostral pole position). **b**, Performance during an example session. Dots represent licks to the right (blue) or the left (red). Grey bars, correct trials; black bars, incorrect trials. S, sample; D, delay; R, response. **c**, Schematic for recording and photostimulation (cyan arrows) configuration for each cell type. **d**, Collision test for an example neuron. Trials with spontaneous spikes preceding the light-evoked spike are shown binned by latency from top to bottom. Putative photostimulation-evoked spikes are at  $\pm \Delta t$ . When a spike occurs in the interval  $[-\Delta t, +\Delta t]$ , a collision occurs with the photostimulation-evoked spike in the axon and the somatic spike at  $+\Delta t$ . **e**, Depth distribution of PT<sub>upper</sub> and PT<sub>lower</sub> neurons based on micromanipulator readings (PT<sub>upper</sub>:  $n = 61$  cells; PT<sub>lower</sub>:  $n = 69$  cells). Depths are measured from the dorsal surface and are uncorrected for the curvature of cortical layers. Error bars represent mean  $\pm$  s.d. **f**, Example identified PT neurons. Top, spike rastergrams for correct lick right trials (blue) and lick left trials (red). Bottom, trial-averaged spike rates.

## Movement commands

Microstimulation of the ALM is sufficient to initiate bouts of directional licking<sup>18,29</sup>, but the rhythmic movements involved in licking and swallowing are coordinated by circuits in the reticular nuclei of the medulla<sup>23,30</sup>. PT<sub>lower</sub> neurons provide a direct path from the ALM to premotor circuits in the medulla (Fig. 2a, b and Extended Data Fig. 2). We reasoned that putative ALM signals driving movement should have selectivity for specific movements and emerge between the go cue and movement onset. In addition, movement commands should lie within an activity subspace that is orthogonal to the direction that predicts movement in the delay epoch; otherwise movement would be triggered prematurely<sup>31,32</sup>.

We determined CD<sub>go</sub> as the direction that maximizes selectivity in the 400 ms immediately after the go cue, orthogonal to CD<sub>late</sub> (Fig. 6a). Along CD<sub>go</sub>, selectivity was larger, emerged faster, and persisted longer in the PT<sub>lower</sub> than in the PT<sub>upper</sub> population (Fig. 6b, c). In the PT<sub>lower</sub>

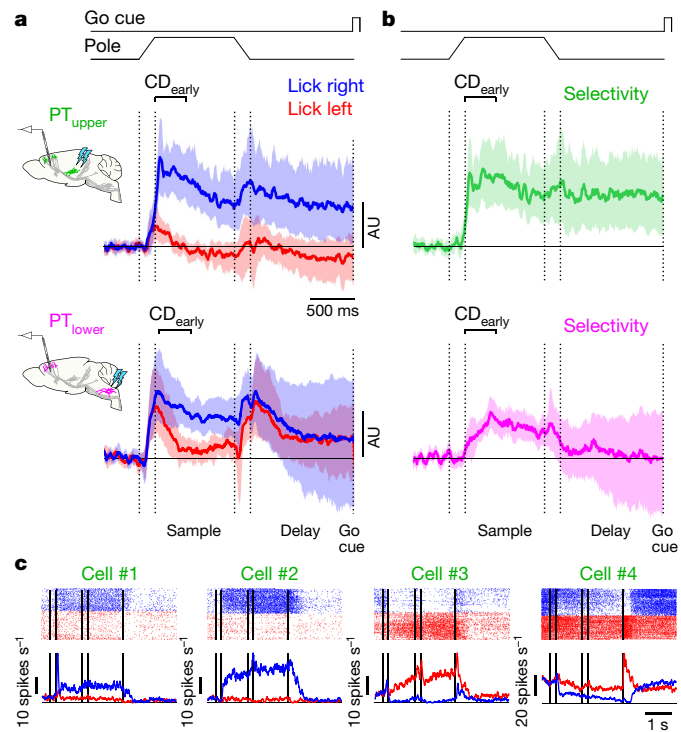


**Fig. 5 | Persistent preparatory activity in PT<sub>upper</sub> neurons.** **a**, Time course of the linear combination of neuronal activity that best differentiates trial type after stimulus onset (CD<sub>early</sub>) on lick right (blue) and lick left (red) trials for PT<sub>upper</sub> (top) and PT<sub>lower</sub> (bottom) neurons. AU, arbitrary units. **b**, Difference in CD<sub>early</sub> projections on lick right and lick left trials (selectivity) in PT<sub>upper</sub> (top; green) and PT<sub>lower</sub> (bottom; magenta) neurons. **c**, Example identified PT<sub>upper</sub> neurons. Top, raster plots for correct lick right trials (blue) and lick left trials (red). Bottom, trial-averaged spike rates. Shaded regions represent the standard deviation of the distribution produced by hierarchical bootstrapping ( $n = 1,000$  iterations) in **a** and 5–95% confidence intervals in **b** (denoting region significantly greater than zero,  $P < 0.05$  one-sided test, bootstrap).

population, significant selectivity emerged 24 ms after the go cue, faster than in the PT<sub>upper</sub> population (48 ms) (Fig. 6c). The onset of the first detectable movement occurred approximately 50 ms after the go cue onset (99% confidence interval: 38–56 ms). The coding direction changed rapidly at the go cue in the PT<sub>lower</sub> population, and more slowly, over several hundred milliseconds, in the PT<sub>upper</sub> population (Extended Data Fig. 7c, e). Individual PT<sub>lower</sub> neurons displayed pronounced changes in selectivity at the go cue (Fig. 6d).

Each bout of licking consists of a sequence of directional tongue protrusions at a stereotyped frequency (approximately 8 Hz; Fig. 4b). Aligning PT<sub>lower</sub> activity to the last lick in a bout revealed additional movement-related features. Selectivity along both CD<sub>late</sub> and CD<sub>go</sub> ceased with the offset of movement (Extended Data Fig. 10a, b), simultaneous with an abrupt change in the coding direction (Extended Data Fig. 10c). This transition was not observed in the dynamics of the PT<sub>upper</sub> population. Indeed, examining the activity of single neurons in the PT<sub>lower</sub> population revealed neurons that were strongly modulated at the go cue, at the offset of movement, or both (Extended Data Fig. 10d)—features rarely observed in PT<sub>upper</sub> cells. These results show that subgroups of PT<sub>lower</sub> neurons have activity patterns consistent with roles in initiating, sustaining, and/or terminating movements.

## Discussion

PT neurons exhibit diverse activity patterns that are related to movement planning and execution<sup>2,4,18,19,32</sup>. We have shown that motor cortex PT neurons comprise two cell types. PT<sub>upper</sub> neurons connect with the thalamus and avoid motor centres in the medulla. These neurons tend to show early and persistent preparatory activity. PT<sub>lower</sub> neurons

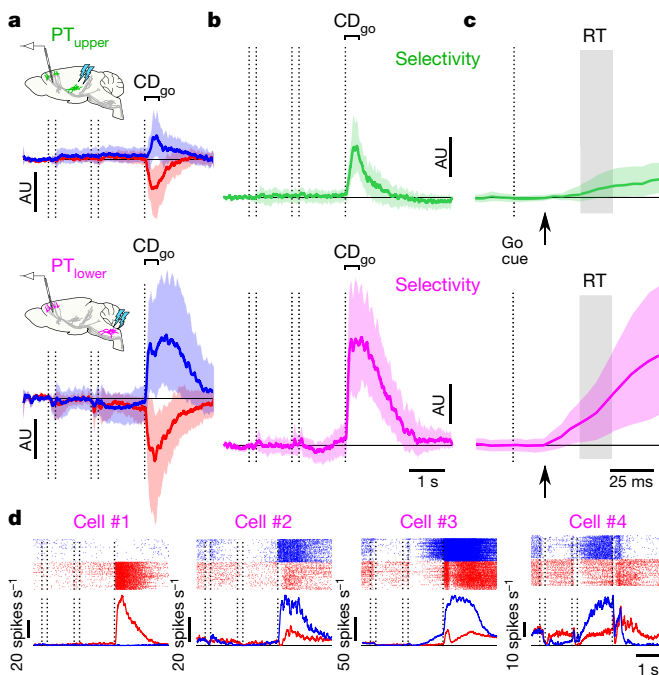


**Fig. 6 | Movement commands in PT<sub>lower</sub> neurons.** **a**, Time course of the linear combination of neuronal activity that best differentiates trial types after the go cue (CD<sub>go</sub>) on lick right (blue) and lick left (red) trials for PT<sub>upper</sub> (top) and PT<sub>lower</sub> (bottom) neurons. **b**, Difference in CD<sub>go</sub> projections on lick right and lick left (selectivity) trials in PT<sub>upper</sub> (top; green) and PT<sub>lower</sub> (bottom; magenta) neurons. **c**, Data from **b** expanded around the go cue. Grey region indicates the distribution of session-averaged reaction times (RT; earliest detected orofacial movement; 99% confidence interval = 38–56 ms). Along CD<sub>go</sub>, selectivity in PT<sub>lower</sub> neurons emerged 24 ms after the go cue, faster than in the PT<sub>upper</sub> population (48 ms) and consistent with role in movement initiation. **d**, Example identified PT<sub>lower</sub> neurons. Top, raster plots for correct lick right trials (blue) and lick left trials (red). Bottom, trial-averaged spike rates. Shaded regions represent the s.d. of the distribution produced by hierarchical bootstrapping ( $n = 1,000$  iterations) in **a** and 5–95% confidence intervals in **b** and **c** (denoting region significantly greater than zero,  $P < 0.05$  one-sided test, bootstrap).

avoid the thalamus and project to motor nuclei in the medulla. These neurons show late preparatory activity and seem to control movement initiation and termination. The segregation of PT neurons into two distinct types persists across the motor cortex and may generalize to other cortical areas<sup>33</sup> and other mammals<sup>34,35</sup>.

Previous studies have suggested that collaterals of PT neurons to the thalamus<sup>13,14</sup> might provide an efference copy of motor commands<sup>36</sup>. Instead, we show that neurons that project to motor centres do not project to the thalamus. Corticothalamic PT<sub>upper</sub> neurons encode more cognitive signals related to motor planning. The thalamus also receives a projection from L6 corticothalamic neurons, but these neurons are sparsely active, uncoupled from PT neurons, and have weak synapses on thalamic neurons<sup>37,38</sup>.

Preparatory activity appeared early and remained persistent in PT<sub>upper</sub> neurons, whereas movement commands were observed in PT<sub>lower</sub> neurons. At the same time, several signals were multiplexed within both populations of PT neurons. For example, preparatory activity emerged in PT<sub>lower</sub> neurons during the delay epoch (along CD<sub>late</sub>) and persisted through the go cue and up to the termination of licking bouts. In the same cell type, and sometimes in the same individual cells (for example, Fig. 6d; cell #3), activity was modulated after the go cue along a different direction (CD<sub>go</sub>), consistent with a movement command. In addition, cell type explained relatively little of the overall variance in neural activity (Extended Data Fig. 6). This highlights that even defined cell types express rich population coding.

Future studies that link detailed anatomy with transcriptional profiling might lead to further subdivision of PT neuron types, particularly the Npsr1-Hpgd PT<sub>upper</sub> cells that mapped to two transcriptomic clusters (Figs. 1, 2). Exploring the connectivity of each PT type with each other and other ALM cell types, as well as long-range inputs, will be crucial for understanding how motor planning and movement signals arise differentially across the PT neuron populations. In addition to PT neurons, the ALM contains 14 transcriptomic clusters corresponding to diverse intratencephalic neurons, which project to other cortical areas and the striatum<sup>21</sup> (Fig. 1). Identifying the roles of other distinct cell types in movement will require experiments similar to those presented here—in addition to mapping the connections between cell types—and are crucial for understanding the function of cortical circuits.

### Online content

Any methods, additional references, Nature Research reporting summaries, source data, statements of data availability and associated accession codes are available at <https://doi.org/10.1038/s41586-018-0642-9>.

Received: 5 December 2017; Accepted: 24 September 2018;

Published online 31 October 2018.

- Svoboda, K. & Li, N. Neural mechanisms of movement planning: motor cortex and beyond. *Curr. Opin. Neurobiol.* **49**, 33–41 (2018).
- Shenoy, K. V., Sahani, M. & Churchland, M. M. Cortical control of arm movements: a dynamical systems perspective. *Annu. Rev. Neurosci.* **36**, 337–359 (2013).
- Evarts, E. V. Pyramidal tract activity associated with a conditioned hand movement in the monkey. *J. Neurophysiol.* **29**, 1011–1027 (1966).
- Kaufman, M. T. et al. The largest response component in the motor cortex reflects movement timing but not movement type. *eNeuro* **3**, <https://doi.org/10.1523/ENEURO.0085-16.2016> (2016).
- Kiritani, T., Wickersham, I. R., Seung, H. S. & Shepherd, G. M. G. Hierarchical connectivity and connection-specific dynamics in the corticospinal-corticostratal microcircuit in mouse motor cortex. *J. Neurosci.* **32**, 4992–5001 (2012).
- Kawaguchi, Y. Pyramidal cell subtypes and their synaptic connections in layer 5 of rat frontal cortex. *Cereb. Cortex* **27**, 5755–5771 (2017).
- Hooks, B. M. et al. Organization of cortical and thalamic input to pyramidal neurons in mouse motor cortex. *J. Neurosci.* **33**, 748–760 (2013).
- von Economo, C. & Parker, S. *The Cytoarchitectonics of the Human Cerebral Cortex* (Oxford University Press, London 1929).
- Kuyper, H. G. J. M. in *Comprehensive Physiology* (ed. Terjung, R.) (John Wiley & Sons, Inc., New Jersey, 1981).
- Lemon, R. N. Descending pathways in motor control. *Annu. Rev. Neurosci.* **31**, 195–218 (2008).
- Cheney, P. D. & Fetz, E. E. Functional classes of primate corticomotoneuronal cells and their relation to active force. *J. Neurophysiol.* **44**, 773–791 (1980).
- Lawrence, D. G. & Kuyper, H. G. The functional organization of the motor system in the monkey. I. The effects of bilateral pyramidal lesions. *Brain J. Neuro.* **91**, 1–14 (1968).
- Deschênes, M., Bourassa, J. & Pinault, D. Corticothalamic projections from layer V cells in rat are collaterals of long-range corticofugal axons. *Brain Res.* **664**, 215–219 (1994).
- Kita, T. & Kita, H. The subthalamic nucleus is one of multiple innervation sites for long-range corticofugal axons: a single-axon tracing study in the rat. *J. Neurosci. Off. J. Soc. Neurosci.* **32**, 5990–5999 (2012).
- Guo, Z. V. et al. Maintenance of persistent activity in a frontal thalamocortical loop. *Nature* **545**, 181–186 (2017).
- Jones, E. G. & Wise, S. P. Size, laminar and columnar distribution of efferent cells in the sensory-motor cortex of monkeys. *J. Comp. Neurol.* **175**, 391–437 (1977).
- Wang, X. et al. Deconstruction of corticospinal circuits for goal-directed motor skills. *Cell* **171**, 440–455.e14 (2017).
- Li, N., Chen, T.-W., Guo, Z. V., Gerfen, C. R. & Svoboda, K. A motor cortex circuit for motor planning and movement. *Nature* **519**, 51–56 (2015).
- Tanji, J. & Evarts, E. V. Anticipatory activity of motor cortex neurons in relation to direction of an intended movement. *J. Neurophysiol.* **39**, 1062–1068 (1976).
- Turner, R. S. & DeLong, M. R. Corticostriatal activity in primary motor cortex of the macaque. *J. Neurosci.* **20**, 7096–7108 (2000).
- Tasic, B. et al. Shared and distinct transcriptomic cell types across neocortical areas. *Nature* <https://doi.org/10.1038/s41586-018-0654-5> (2018).
- Economo, M. N. et al. A platform for brain-wide imaging and reconstruction of individual neurons. *eLife* **5**, e10566 (2016).
- Stanek, E., IV, Cheng, S., Takatoh, J., Han, B.-X. & Wang, F. Monosynaptic premotor circuit tracing reveals neural substrates for oro-motor coordination. *eLife* **3**, e02511 (2014).
- Tervo, D. G. et al. A designer AAV variant permits efficient retrograde access to projection neurons. *Neuron* **92**, 372–382 (2016).
- Guo, Z. V. et al. Flow of cortical activity underlying a tactile decision in mice. *Neuron* **81**, 179–194 (2014).
- Chen, T.-W., Li, N., Daie, K. & Svoboda, K. A map of anticipatory activity in mouse motor cortex. *Neuron* **94**, 866–879 (2017).

27. Li, N., Daie, K., Svoboda, K. & Druckmann, S. Robust neuronal dynamics in premotor cortex during motor planning. *Nature* **532**, 459–464 (2016).
  28. Cunningham, J. P. & Yu, B. M. Dimensionality reduction for large-scale neural recordings. *Nat. Neurosci.* **17**, 1500–1509 (2014).
  29. Komiyama, T. et al. Learning-related fine-scale specificity imaged in motor cortex circuits of behaving mice. *Nature* **464**, 1182–1186 (2010).
  30. Travers, J. B., Dinardo, L. A. & Karimnamazi, H. Motor and premotor mechanisms of licking. *Neurosci. Biobehav. Rev.* **21**, 631–647 (1997).
  31. Druckmann, S. & Chklovskii, D. B. Neuronal circuits underlying persistent representations despite time varying activity. *Curr. Biol.* **22**, 2095–2103 (2012).
  32. Kaufman, M. T., Churchland, M. M., Ryu, S. I. & Shenoy, K. V. Cortical activity in the null space: permitting preparation without movement. *Nat. Neurosci.* **17**, 440–448 (2014).
  33. Hattox, A. M. & Nelson, S. B. Layer V neurons in mouse cortex projecting to different targets have distinct physiological properties. *J. Neurophysiol.* **98**, 3330–3340 (2007).
  34. Catsman-Berrevoets, C. E. & Kuypers, H. G. A search for corticospinal collaterals to thalamus and mesencephalon by means of multiple retrograde fluorescent tracers in cat and rat. *Brain Res.* **218**, 15–33 (1981).
  35. Steriade, M. & Yossif, G. Afferent and recurrent collateral influences on cortical somatosensory neurons. *Exp. Neurol.* **56**, 334–360 (1977).
  36. Sherman, S. M. Thalamus plays a central role in ongoing cortical functioning. *Nat. Neurosci.* **19**, 533–541 (2016).
  37. Yamawaki, N. & Shepherd, G. M. G. Synaptic circuit organization of motor corticothalamic neurons. *J. Neurosci.* **35**, 2293–2307 (2015).
  38. Sherman, S. M. & Guillory, R. W. On the actions that one nerve cell can have on another: distinguishing “drivers” from “modulators”. *Proc. Natl Acad. Sci. USA* **95**, 7121–7126 (1998).
- Acknowledgements** We thank A. Lemire and K. Aswath for single-cell sorting and bulk RNA-seq, S. Lindo for stereotaxic surgeries, D. Kao and T. Wang for help with RNA-seq analysis, D. Alcor for imaging assistance, and N. Li and H. Inagaki for help with electrophysiological recordings and for discussion. We thank M. Cembrowski, E. Bloss and F. Henry for discussion. H. Inagaki, M. Sherman, S. Romani, L. Luo, G. Shepherd and T. Wang provided comments on the manuscript. Imaging and reconstructions of neuronal morphology was performed by the Janelia MouseLight project (<http://mouselight.janelia.org/>). This work was funded by the Howard Hughes Medical Institute, the Allen Institute for Brain Science, the NIH Brain Initiative (U01MH105982 to H.Z.), and the Intramural Research Program of the NIMH (ZIA-MH002497-29 to C.R.G.).

**Reviewer information** *Nature* thanks P. Carninci, M. Fee, T. Mrsic-Flogel and the anonymous reviewer(s) for their contribution to the peer review of this work.

**Author contributions** M.N.E., K.S., S.V., L.L.L., B.T. and H.Z.: conception and design of the experiments. B.T., L.T.G., T.N.N., K.A.S., Z.Y. and H.Z.: scRNA-seq experiments, with material provided by M.N.E., S.V. and L.W. M.N.E., E.B., J.W. and J.C.: single neuron reconstructions. S.V., C.R.G. and M.N.E.: in situ experiments and analysis. M.N.E.: electrophysiology experiments. M.N.E., S.V. and C.R.G.: anatomical experiments. M.N.E., S.V., V.M., L.T.G., Z.Y., K.S. and L.L.L.: data analysis. M.N.E., K.S. and L.L.L.: wrote the paper with input from all authors.

**Competing interests** The authors declare no competing interests.

#### Additional information

**Extended data** is available for this paper at <https://doi.org/10.1038/s41586-018-0642-9>.

**Supplementary information** is available for this paper at <https://doi.org/10.1038/s41586-018-0642-9>.

**Reprints and permissions information** is available at <http://www.nature.com/reprints>.

**Correspondence and requests for materials** should be addressed to K.S.

**Publisher's note:** Springer Nature remains neutral with regard to jurisdictional claims in published maps and institutional affiliations.

## METHODS

**Animals.** Mice used for scRNA-seq experiments in the visual cortex and ALM are described elsewhere<sup>21</sup>. Mice used for all other experiments are listed in Supplementary Tables 2 and 3. Mice were housed on a 12-h light/dark cycle with ad libitum access to food and water, except during behaviour (described in the ‘Mouse behaviour’ section). For electrophysiological experiments, group sizes were based on the number of identified neurons possible to record in each animal (5–20) and the number of cells likely to yield interpretable results (>50 neurons per condition; based on previous work<sup>18</sup>). For sequencing and anatomy experiments, sample sizes were similar to those used by others in the field. No statistical tests were used to determine sample sizes.

**Surgical procedures.** All procedures were in accordance with protocols approved by the Janelia Research Campus Institutional Animal Care and Use Committee and Institutional Biosafety Committee. Mice were given buprenorphine HCl (0.1 mg kg<sup>-1</sup>; Bedford Laboratories) and ketoprofen (5 mg kg<sup>-1</sup>; Fort Dodge Animal Health) for post-operative analgesia and to reduce inflammation. Surgical procedures were carried out under 1–2% isoflurane anaesthesia. Mice were placed in a stereotaxic headholder on a thermal blanket and their eyes covered with artificial tears (Rugby). Marcaine (0.05 ml, 0.5%) was injected under the skin covering the skull. The skin and periosteum covering the skull was removed and the skull thinned overlying the sites of viral injection(s). For all injections, virus was injected using a manual volume displacement injector (MMO-220A, Narishige) connected to a glass pipette (5-000-2005, Drummond Scientific) pulled to a 30 µm tip (P-2000, Sutter Instruments) that was bevelled to a sharp tip. Pipettes were back-filled with mineral oil and virus was front-loaded before injection. Pipettes were inserted through the thinned bone to the appropriate depth and virus injected at 10 nL min<sup>-1</sup>. For electrophysiology, a fibre optic cannula (CFML12L05; Thorlabs) was implanted 200 µm above the viral injection target and a headbar implanted caudal to Bregma. Dental acrylic (Jet repair; Pearson Dental) was used to secure the optic fibre and headbar to the skull and protect exposed bone.

**Viral expression.** All viruses used in these experiments were adeno-associated viruses (AAVs) produced in the Janelia Research Campus (JRC) Virus Shared Resource. Viruses used for scRNA-seq experiments are described elsewhere<sup>21</sup>. For all other experiments, viruses incorporated the rAAV2-retro capsid<sup>24</sup>, with the exception of axonal reconstruction experiments (Fig. 2a, b and Extended Data Fig. 2a–d), which used AAV2 serotype 1. Viruses used, viral titres, injection volumes, injection coordinates, and associated experiments are described in Supplementary Tables 2 and 4.

**scRNA-seq.** Single-cell RNA-seq data (Figs. 1a, b, 2e, f and 3a and Extended Data Figs. 1a, b and 4a–c, h, i), were collected and analysed as described elsewhere<sup>21</sup>. A total of 9,573 scRNA-seq transcriptomes were measured from ALM neurons (4,477 glutamatergic) and 14,249 from V1 neurons. To collect individual cells, layer-enriching dissections were used from brains of pan-neuronal, pan-excitatory or pan-inhibitory recombinase lines crossed to recombinase reporters (10,752 cells). This dataset was supplemented with 10,414 cells isolated from other recombinase lines. Dissections without layer enrichment, or multiple layers combined, were used for lines with sparse labelling. Additional recombinase lines were selected to capture cellular diversity that was suggested by ongoing analysis of the data. In total, 2,656 additional cells were derived from viral retrograde labelling, with the goal to establish correspondence between transcriptomic types and projection properties. PT neurons were collected from retrogradely-labelled brains ( $n=62$  medulla injection;  $n=94$  thalamus;  $n=100$  pons;  $n=97$  superior colliculus;  $n=2$  amygdala;  $n=2$  zona incerta) and recombinase crosses ( $n=10$ ).

**scRNA-seq analysis.** A detailed description of scRNA-seq analysis is provided elsewhere<sup>21</sup>. In brief, 50-base pair paired-end reads were aligned to GRCm38 (mm10) using a RefSeq annotation gff file retrieved from NCBI on 18 January 2016 ([https://www.ncbi.nlm.nih.gov/genome/annotation\\_euk/all/](https://www.ncbi.nlm.nih.gov/genome/annotation_euk/all/)). Sequence alignment was performed using STAR v2.5.3<sup>48</sup> in two-pass mode. Transcriptomic features, extracted by weighted gene co-expression network analysis<sup>39</sup>, were clustered in an iterative and bootstrapped manner. The output of this procedure is a co-clustering matrix, which shows the frequency with which any cell clusters with any other cell in 100 bootstrapped iterative clustering rounds. The transcriptomic clusters are defined by ‘cutting’ the co-clustering matrix to derive membership of each cell to a cluster. The membership of each cell is tested post-clustering by classification algorithms to assign core versus intermediate identity to cells<sup>40</sup>. Cells that were reliably assigned to only one cluster are ‘core’ cells (21,195); cells that were assigned to more than one cluster (typically two) are ‘intermediate’ cells (2,627 cells). ALM scRNA-seq transcriptomes clustered into 27 glutamatergic, 61 GABAergic and 16 non-neuronal types. In scRNA-seq experiments, differentially expressed genes (Fig. 3a and Extended Data Fig. 1a, c) were detected as described previously<sup>40</sup> using the R package limma v3.30.13<sup>41</sup>. In brief, differentially expressed genes were defined as genes with more than twofold change and adjusted  $P < 0.01$ , and with expression following a bimodal pattern confined to one cluster relative to the other. Multiple genes were found satisfying criteria for markers. Cluster

names (for example, *Slco2a1*, *Npsr1* and *Hpgd*) were selected from candidate genes as those adding the most discriminability for adjacent leafs of the dendrogram and that were detected in more than 50% of individual cells with preference for globally unique genes<sup>21</sup>.

**Single-cell axonal reconstruction.** The axons of single neurons were labelled and imaged as described previously<sup>22</sup> (Fig. 2a, b and Extended Data Fig. 2a–d). Neurons in the motor cortex were sparsely labelled using a viral vector encoding either GFP or tdTomato. At least 3 weeks after virus injection, mice were perfused and brains extracted. Brains were embedded in gelatin and cleared using a combination of DMSO and D-sorbitol. The full volume of each brain was imaged at sub-micrometre resolution using a block-face two-photon microscope with integrated vibratome. Individual neurons were reconstructed manually in three-dimensions using the Janelia Workstation (<https://www.janelia.org/confocal-imagery-management-and-analysis-tools>) by two independent annotators who were blinded to all analyses. Consensus reconstructions were determined by resolving discrepancies (generally <5%) between annotators. Each dataset was registered to the Allen Common Coordinate Framework<sup>42</sup> using landmark based registration (3DSlicer, Landmark Registration module) and a thin plate spline warp determined between the two image spaces. Neuronal reconstructions were then projected into the reference space to determine the brain area associated with each axonal segment, branch point, and terminus.

**Histology and imaging.** At least two weeks after viral injections, mice were transcardially perfused with PBS (>20 ml) followed by 4% paraformaldehyde (>20 ml). Brains were post-fixed overnight. For immunolabelling (Fig. 2c, d and Extended Data Fig. 3), brains were transferred to a 20% sucrose solution for cryoprotection and sectioned coronally at 50 µm on a freezing microtome. In all other cases (Extended Data Fig. 2e), brains were sectioned at 50 or 100 µm on a vibratome (VT1200; Leica Biosystems). Sections were processed using standard immunohistochemical techniques and imaged as previously described<sup>43</sup> (Fig. 2c, d and Extended Data Figs. 2e, 3). Brightness and contrast were adjusted manually to match approximate luminance values across imaging experiments in a linear fashion using ImageJ/Fiji.

**Bulk RNA-seq.** Cells retrogradely labelled from the thalamus, medulla, pons, and superior colliculus with GFP or tdTomato were collected by manual cell sorting<sup>44</sup> (Extended Data Figs. 1c, d, 4d–g, i). Approximately 50–120 cells were collected per sample, with 7 biological replicates performed each for thalamus and medulla and 3 replicates each for superior colliculus and pons. Cells were isolated by manual cell sorting on a fluorescence dissecting scope, following micro-dissection, trituration and enzymatic digestion as described previously<sup>45</sup>. Following pooling and lysis, total RNA was extracted by Picopure kit (KIT0204; Thermo-Fisher). Amplified DNA was produced using Ovation RNA-seq System V2 kit (7102; NuGEN), fragmented to ~200 bp, ligated to Illumina sequencing adaptors with Encore Rapid kit (0314; NuGEN), and sequenced on an Illumina HiSeq 2500 with fourfold multiplexing (single end, 100–bp read length).

**Bulk RNA-seq analysis.** Adaptor sequences (AGATCGGAAGAGCACA CGTCTGAACTCCAGTCAC) were removed from reads using Trimmomatic 0.36<sup>46</sup>, mapped using STAR 2.5.3a<sup>47</sup> to the Ensembl mouse genome GRCm38.p5, release 90 (<https://www.ensembl.org>). Mapped reads were normalized to the total number of reads per sample (counts per million). Principal components analysis of the 7 thalamus-projecting and 7 medulla-projecting replicates showed that a single replicate from each behaved as an outlier. Thus, for further analysis, 6 replicates were considered for each. Three replicates were performed for both superior colliculus-projecting and pons-projecting neurons with all replicates used in further analysis. Similar numbers of genes were detected in each of the bulk RNA-seq samples (thalamus: 12,317; medulla: 12,363). These numbers were higher than the genes detected across all cells in scRNA-seq (Extended Data Fig. 4e–h). In bulk RNA-seq experiments, differential expression analysis was performed using EdgeR<sup>48</sup>. Genes were determined to be differentially expressed (Extended Data Fig. 1b, d) between  $\text{PT}_{\text{upper}}$  and  $\text{PT}_{\text{lower}}$  cells according to the following criteria: false discovery rate of  $1 \times 10^{-5}$ , mean expression fold change  $>2$ , and non-zero expression in at least 5 of 6 replicates. A number of potential marker genes were identified for both  $\text{PT}_{\text{upper}}$  and  $\text{PT}_{\text{lower}}$  neurons from both scRNA-seq and bulk RNA-seq (Extended Data Figs. 1, 4i). *Slco2a1*, the gene selected as the name for the  $\text{PT}_{\text{lower}}$  cluster from scRNA-seq data, was confirmed as having high expression in  $\text{PT}_{\text{lower}}$  neurons and low expression in  $\text{PT}_{\text{upper}}$  neurons (Fig. 3 and Extended Data Fig. 1a, c) and was thus chosen as a marker gene for  $\text{PT}_{\text{lower}}$  neurons. *Npnt* was chosen as a marker gene for  $\text{PT}_{\text{upper}}$  neurons as it was highly expressed across both the *Npsr1* and *Hpgd* clusters and was differentially expressed in both scRNA-seq and bulk RNA-seq as well, with little expression in other layer 5 and 6 clusters, GABAergic neurons, and glia.

**In situ hybridization.** Animals were perfused with 4% paraformaldehyde and brains were post-fixed in 4% paraformaldehyde overnight at 4 °C. Brains were then rinsed in PBS and cryoprotected in 30% sucrose, and 20-µm thick sections were cut on a cryostat. smFISH (RNAscope) followed by immunohistochemistry was

performed on fixed frozen tissue from mice injected with rAAV2-retro-GFP in either the thalamus or medulla (Supplementary Tables 2–4) as per protocols for fixed frozen tissue using proprietary probes from Advanced Cell Diagnostics (ACDBio). Probes used in this study (Mm-Npnt: 316771; Mm-Slco2a1: 485041) were detected using proprietary detection reagent (RNAscope Fluorescent Multiplex Detection Reagents, 320851), using Amp4 Alt B (Atto 550). After smFISH, sections were rinsed in PBS, and blocking buffer (2% BSA and 0.3% serum) was applied for 5 min. Primary antibody (Aves-Labs, GFP-1020) was diluted in the blocking buffer (1:100) and incubated overnight at 4 °C. Sections were rinsed in PBS three times (5 min) and incubated with secondary antibody goat anti-chicken AF 488 (A-11039, Invitrogen; diluted 1:100 in blocking buffer) at room temperature for 2 h. Sections were then rinsed in PBS and coverslips were added with Vectashield containing DAPI (H-1500; VectorLabs). Images were acquired as 7-μm thick stacks collected using a 40×/1.3 numerical aperture (NA) objective (pixel size, 0.11 × 0.11 μm) on a Zeiss 880 inverted confocal microscope. Punctate mRNA signal was quantified on cell volumes from maximum intensity projection of the Z-stacks in the ALM and primary motor cortex (AP: 0.0 to +1.0, ML: 1.0 to 2.0) using Neurolucida (MBF). Single image planes are illustrated in Fig. 3b.

**Mouse behaviour.** Mice were water-restricted and housed on a 12-h reverse light/dark cycle with testing during the dark phase. On days in which mice were not trained, they received 1 ml of water. Behavioural experiments lasted 1–2 h per day, during which mice consumed their daily water intake (approximately 0.5–1.0 ml). Mice unable to sustain stable body weight were given supplementary water. Mice were trained using operant conditioning as previously described<sup>25,49</sup> until reaching behavioural criterion (>75% trials correct). At the beginning of each trial, a vertical pole moved within reach of the whiskers (200-ms travel time). The pole remained in position for 1.0 s and then was retracted (200-ms travel time). The sample epoch was defined as the 1.0 s during which the pole was in range of the whiskers and stationary. After the pole was removed, the mouse was trained to refrain from licking for an additional 1.3 s (delay epoch) before an auditory ‘go cue’ (pure tone, 3.4 kHz, 0.1 s duration) instructed the mouse to lick (reward epoch). Premature licks during the sample or delay epoch resulted in a restart of the requisite epoch and these trials were excluded from all analyses. Licking the correct lick port after the go cue led to a small water reward (3 μl). Licking the incorrect lick port triggered a timeout (2–10 s). Trials in which mice did not lick within a 1.5-s window after the go cue were rare and typically occurred at the end of a session.

**Videography.** Video was acquired at 400 Hz framerate from below and to the side of the mouse using CMOS cameras (CM3-U3-13Y3M, FLIR) with a 4–12 mm focal length lens (12VM412ASIR, Tamron). Camera data were acquired using BIAS (IORodeo). Reaction times were determined by measuring the luminance change in a small region of interest manually placed just below the jaw in side-view movies. Luminance traces were averaged across all of the trials within each session (453 ± 79, mean ± s.d.; range: 295–551). 95% confidence intervals for reaction time were calculated by bootstrapping session means across mice ( $n = 3$ ) and sessions ( $n = 14$ ). Little inter-animal variation was observed in session-averaged reaction time.

**Electrophysiology.** A small craniotomy (diameter, 0.5–1 mm) was made over ALM (AP: 2.5, ML 1.5) one day before the first recording session. Extracellular spikes were recorded using silicon probes containing two shanks each with 32 channels with 25 μm spacing (H2; Cambridge Neurotech). The 64-channel voltage signals were multiplexed, recorded on a PCI6133 board (National Instrument), and digitized at 14 bits. The signals were demultiplexed into the 32 voltage traces, sampled at 25 kHz and stored for offline analyses. A total of 4–7 recordings were made from each craniotomy on consecutive days. The tissue was allowed to settle for 10 min before recording.

To optogenetically tag PT<sub>upper</sub> and PT<sub>lower</sub> neurons during recording, we expressed ChR2-YFP or ChR2(H134R)-GFP selectively in each population using a viral injection into the medulla or thalamus as described above. During each recording session, more than 1,200 photostimuli were delivered at 4 Hz just before and after the behavioural session. Photostimuli were 0.1–0.5 ms at 80–100 mW (measured just before the implanted fibre optic cannula). Reliable antidromic activation was observed in 1–6 units per session. Owing to the proximity of the cerebral peduncle, subthalamic nucleus and zona incerta, which contain projections from both cell types, a smaller viral injection was performed in the thalamus (50 nl) than in the medulla (50–200 nl), resulting in fewer tagged PT<sub>upper</sub> neurons per mouse. Across all sessions recording PT<sub>upper</sub> neurons, mouse performance was 85.4 ± 7.8% on lick left trials and 89.3 ± 9.4% on lick right trials (mean ± s.d.;  $n = 37$  sessions in 8 mice; left hemisphere). In PT<sub>lower</sub> neuron recordings, performance was 83.5 ± 6.3% on lick left trials and 86.3 ± 8.2% on lick right trials ( $n = 23$  sessions in 4 mice; both hemispheres). Mice performed a median of 107 and 105 correct trials on lick left and lick right trials respectively in PT<sub>upper</sub> recordings and 117 and 108 correct trials during PT<sub>lower</sub> recordings. PT neurons recorded from the left and right ALM did not differ and were combined in all further analysis to increase statistical power.

In addition, 495 unidentified single units were isolated from 15 sessions from the same cohort of animals in which PT<sub>upper</sub> neurons were tagged, and 511 unidentified single units were isolated from 14 sessions from the same cohort in which PT<sub>lower</sub> neurons were identified. Unidentified neurons were isolated in the same proportion as tagged neurons across animals. To produce depth-matched samples of unidentified neurons (Extended Data Fig. 8), we restricted analysis to experiments from the left ALM because recordings from the right ALM were made using oblique penetration angles and were biased towards deep L5b. By contrast, recordings from left ALM were obtained with penetrations perpendicular to cortical layers.

**Electrophysiology data analysis.** Extracellular recordings were band-pass filtered (300–4,500 Hz; second order Butterworth filter) and the common mode on ±4 sites was subtracted from each channel. Events were detected using JRClust<sup>50</sup> and spikes from tagged units ( $n = 143$ ) were sorted manually using a custom program written in MATLAB. All other units were sorted using JRClust<sup>50</sup>. Extreme care was taken to restrict analysis to tagged units that could be sorted with a low number of false positive spikes (mean inter-spike intervals less than 2 ms = 0.02%; Extended Data Fig. 5) so that neuronal responses could be faithfully attributed to the correct cell type. Despite this, spike rates were similar to those measured in other ALM recordings in the same task<sup>18</sup> indicating that the false negative spike rate remained low. Information from 4–7 adjacent recording sites was used for sorting each unit. Units recorded during behavioural sessions in which performance was not greater than 65% for both trial types were excluded from the dataset. Units recorded during behavioural sessions with less than 50 correct trials of each type were excluded (13 units were rejected; 130 were kept for further analysis). Unit depths (Fig. 4e) were inferred from manipulator readings only without correction for the angle between the electrode penetration and the orientation of cortical layers. Collision tests were performed for all tagged units to confirm axonal projections to the thalamus or medulla<sup>18,51</sup> (Fig. 4d). Trial-averaged spike rates were calculated in 5 ms time bins and filtered using a causal 50 ms boxcar filter.

The coding direction vector (**CD**) (Figs. 5, 6 and Extended Data Figs. 7, 8, 10) was calculated as:

$$\mathbf{v} = \frac{\bar{x}_{\text{lick right}} - \bar{x}_{\text{lick left}}}{\sqrt{\text{Var}(\bar{x}_{\text{lick right}}) + \text{Var}(\bar{x}_{\text{lick left}})}} \quad (1)$$

$$\mathbf{CD} = \frac{\mathbf{v}}{\sum |\mathbf{v}|} \quad (2)$$

For each neuron, the mean difference in spike rate between lick right,  $\bar{x}_{\text{lick right}}$ , and lick left trials,  $\bar{x}_{\text{lick left}}$ , was calculated in a 400-ms time interval. This vector was divided by the square root of the sum of the across-trial variances of spike rate for each trial type. The resulting vector ( $\mathbf{v}$ ) was then normalized by its  $L_1$  norm so that projections would not scale with vector length (number of cells in population) to produce the coding direction, **CD**. Coding directions were calculated in the first 400 ms of the sample epoch ( $\mathbf{CD}_{\text{early}}$ ; 2.5 to 2.1 s before the go cue) the last 400 ms of the delay epoch ( $\mathbf{CD}_{\text{late}}$ ; 0.4 to 0.0 s before the go cue) and the first 400 ms of the response epoch ( $\mathbf{CD}_{\text{go}}$ ; 0.0 to 0.4 s after the go cue).  $\mathbf{CD}_{\text{go}}$  was orthogonalized to  $\mathbf{CD}_{\text{late}}$  using the Gram–Schmidt process to isolate selectivity emerging after the go cue, independent of the component of  $\mathbf{CD}_{\text{late}}$  that persisted into the response epoch. Coding directions were calculated separately for the PT<sub>upper</sub> and PT<sub>lower</sub> populations.

Projections of the activity of each PT population along the coding directions ( $\mathbf{p}_{\text{lick right}}, \mathbf{p}_{\text{lick left}}$ ) were calculated as:

$$\mathbf{p}_{\text{lick right}} = \mathbf{CD}^T \mathbf{x}_{\text{lick right}} \quad (3)$$

$$\mathbf{p}_{\text{lick left}} = \mathbf{CD}^T \mathbf{x}_{\text{lick left}} \quad (4)$$

Selectivity ( $S$ ) along each direction was:

$$S = \mathbf{p}_{\text{lick right}} - \mathbf{p}_{\text{lick left}} \quad (5)$$

In all cases (Figs. 5, 6 and Extended Data Figs. 7, 8, 10), the illustrated projections are the results of a hierarchical bootstrapping procedure. For each population, 1,000 bootstrapped projections were calculated. For each repetition,  $M$  mice were chosen with replacement from the appropriate cohort, in which  $M$  was the original cohort size. From that sample of mice,  $n$  neurons were randomly chosen (with replacement), in which  $n$  was the number of neurons in the population. For each neuron, 50 correct trials of each trial type were randomly selected with replacement. In all figures, solid lines represent the median and s.d. of all repetitions for projections of the data for each trial type<sup>52,53</sup>. For selectivity, shaded areas represent 5–95% confidence intervals, thereby indicating where projections are significantly different from zero ( $P < 0.05$ , one-sided test, bootstrap).

To determine the variance explained by cell type in Extended Data Fig. 6, trial-averaged activity patterns from all neurons were *z*-scored and time series from trial types were concatenated. These concatenated time series were decomposed separately across each PT population using principal component analysis and the fraction of variance of the data explained by each principal component was calculated. For comparison, we repeated the same procedure, but drew a size-matched sample from the population of unidentified neurons (without replacement). 1,000 repetitions of this procedure were performed to build a distribution for comparison.

To create matrices of the coding direction correlation across time (Extended Data Figs. 7c, 10c), coding directions were calculated at each time point from the trial-averaged spike rates of all neurons within a population (5-ms time bins, filtered using a causal 50-ms boxcar filter), as above, but were normalized by their Euclidean norms to produce unit vectors. Correlation matrices represent the inner product of coding direction vectors at each pair of time points.

Single-cell trial type decoding accuracy (Extended Data Fig. 9) was determined using the average spike rate during the first 400 ms of the sample epoch (2.5 to 2.1 s before the go cue). A spike rate threshold was determined that best distinguished lick right trials from lick left trials (maximal accuracy) with accuracy defined as the proportion of trials correctly classified. Accuracy was  $\geq 50\%$  by definition. Shaded regions in around the cumulative distribution function in Extended Data Fig. 9b, d represent s.e.m., estimated using Greenwood's formula.

All two-sample *t*-tests were Student's *t*-tests.

**Randomization and blinding.** In all experiments in which PT<sub>upper</sub> and PT<sub>lower</sub> neurons were compared in different animals (electrophysiology, *in situ* hybridization, etc.), individual mice were allocated randomly into experimental groups.

Retrogradely labelled neurons were isolated for scRNA-seq by a technician and/or sorted automatically using FACS. Single-neuron reconstructions were performed by expert annotators without knowledge of the biological focus of this study. For electrophysiological recordings, trial types were randomly determined by a computer program. During spike sorting, experimenters did not have access to trial type, and individual events could not be related to trial epochs so experimenters were blinded to conditions.

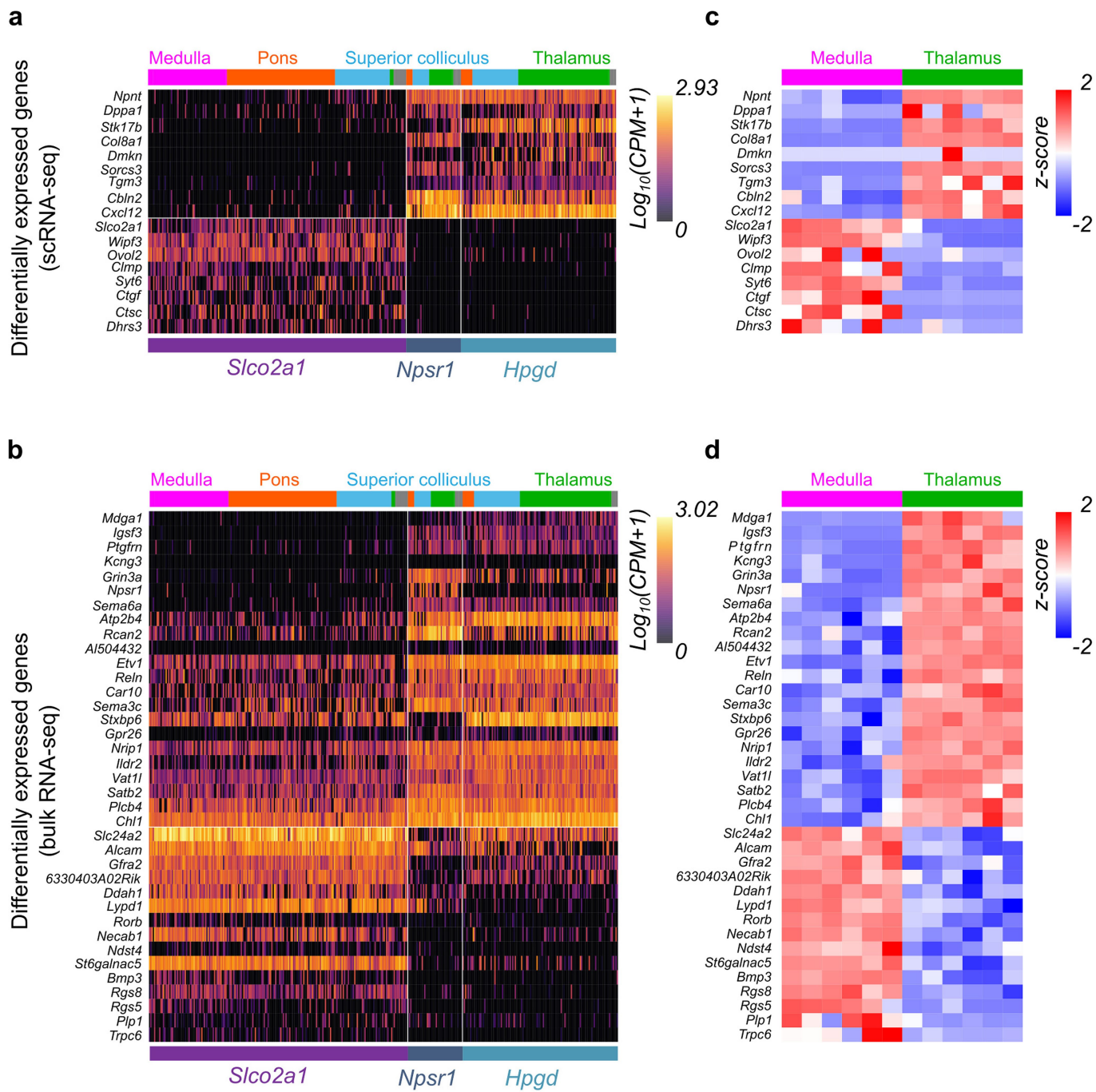
**Reporting summary.** Further information on research design is available in the Nature Research Reporting Summary linked to this paper.

**Code availability.** Analysis code is available at <https://github.com/SvobodaJanelia>.

## Data availability

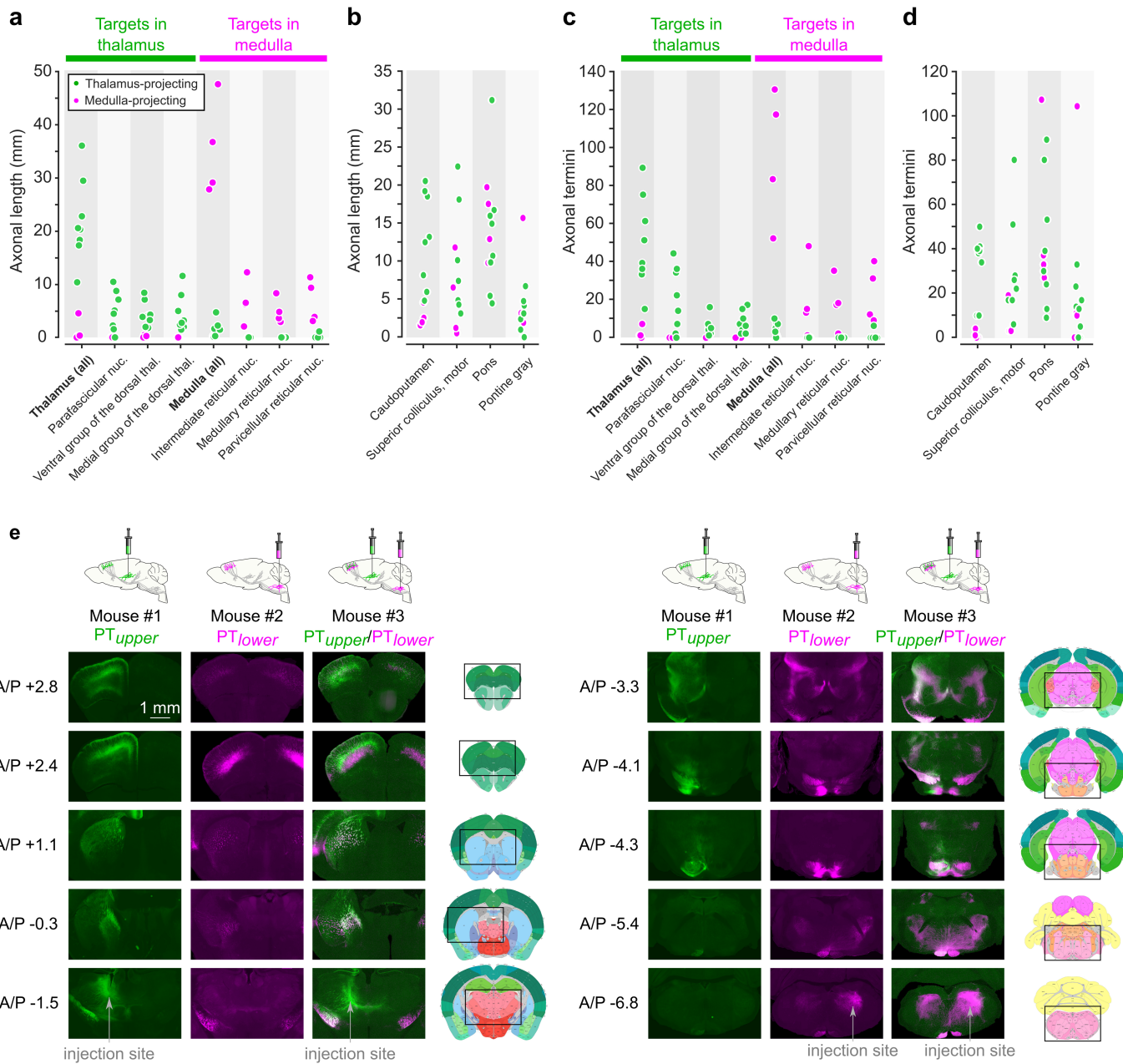
The full single-cell RNA-seq dataset has been described previously<sup>21</sup>. Bulk RNA-seq data are available at the Gene Expression Omnibus (GEO) under accession GSE119182. Electrophysiology data are available at CRCNS.org and Figshare (doi: 10.25378/janelia.7007846).

39. Langfelder, P. & Horvath, S. WGCNA: an R package for weighted correlation network analysis. *BMC Bioinformatics* **9**, 559 (2008).
40. Tasic, B. et al. Adult mouse cortical cell taxonomy revealed by single cell transcriptomics. *Nat. Neurosci.* **19**, 335–346 (2016).
41. Ritchie, M. E. et al. limma powers differential expression analyses for RNA-sequencing and microarray studies. *Nucleic Acids Res.* **43**, e47 (2015).
43. Oh, S. W. et al. A mesoscale connectome of the mouse brain. *Nature* **508**, 207–214 (2014).
44. Paletzki, R. & Gerfen, C. R. Whole mouse brain image reconstruction from serial coronal sections using FIJI (ImageJ). *Curr. Protoc. Neurosci.* **73**, 1.25.1–1.25.21 (2015).
45. Sugino, K. et al. Molecular taxonomy of major neuronal classes in the adult mouse forebrain. *Nat. Neurosci.* **9**, 99–107 (2006).
46. Sugino, K. et al. Cell-type-specific repression by methyl-CpG-binding protein 2 is biased toward long genes. *J. Neurosci.* **34**, 12877–12883 (2014).
47. Bolger, A. M., Lohse, M. & Usadel, B. Trimmomatic: a flexible trimmer for Illumina sequence data. *Bioinformatics* **30**, 2114–2120 (2014).
48. Dobin, A. et al. STAR: ultrafast universal RNA-seq aligner. *Bioinformatics* **29**, 15–21 (2013).
49. McCarthy, D. J., Chen, Y. & Smyth, G. K. Differential expression analysis of multifactor RNA-Seq experiments with respect to biological variation. *Nucleic Acids Res.* **40**, 4288–4297 (2012).
50. Guo, Z. V. et al. Procedures for behavioral experiments in head-fixed mice. *PLoS One* **9**, e88678 (2014).
51. Jun, J. J. et al. Real-time spike sorting platform for high-density extracellular probes with ground-truth validation and drift correction. Preprint at <https://www.biorxiv.org/content/early/2017/01/19/101030> (2017).
52. Towe, A. L., Patton, H. D. & Kennedy, T. T. Response properties of neurons in the perirhinal cortex of the cat following electrical stimulation of the appendages. *Exp. Neurol.* **10**, 325–344 (1964).
53. Aarts, E., Verhage, M., Veenvliet, J. V., Dolan, C. V. & van der Sluis, S. A solution to dependency: using multilevel analysis to accommodate nested data. *Nat. Neurosci.* **17**, 491–496 (2014).
54. van der Leeden, R. in *Handbook of Multilevel Analysis* (eds de Leeuw, J. & Meijer, E.) 401–433 (Springer, New York, 2008).
55. Lein, E. S. et al. Genome-wide atlas of gene expression in the adult mouse brain. *Nature* **445**, 168–176 (2007).



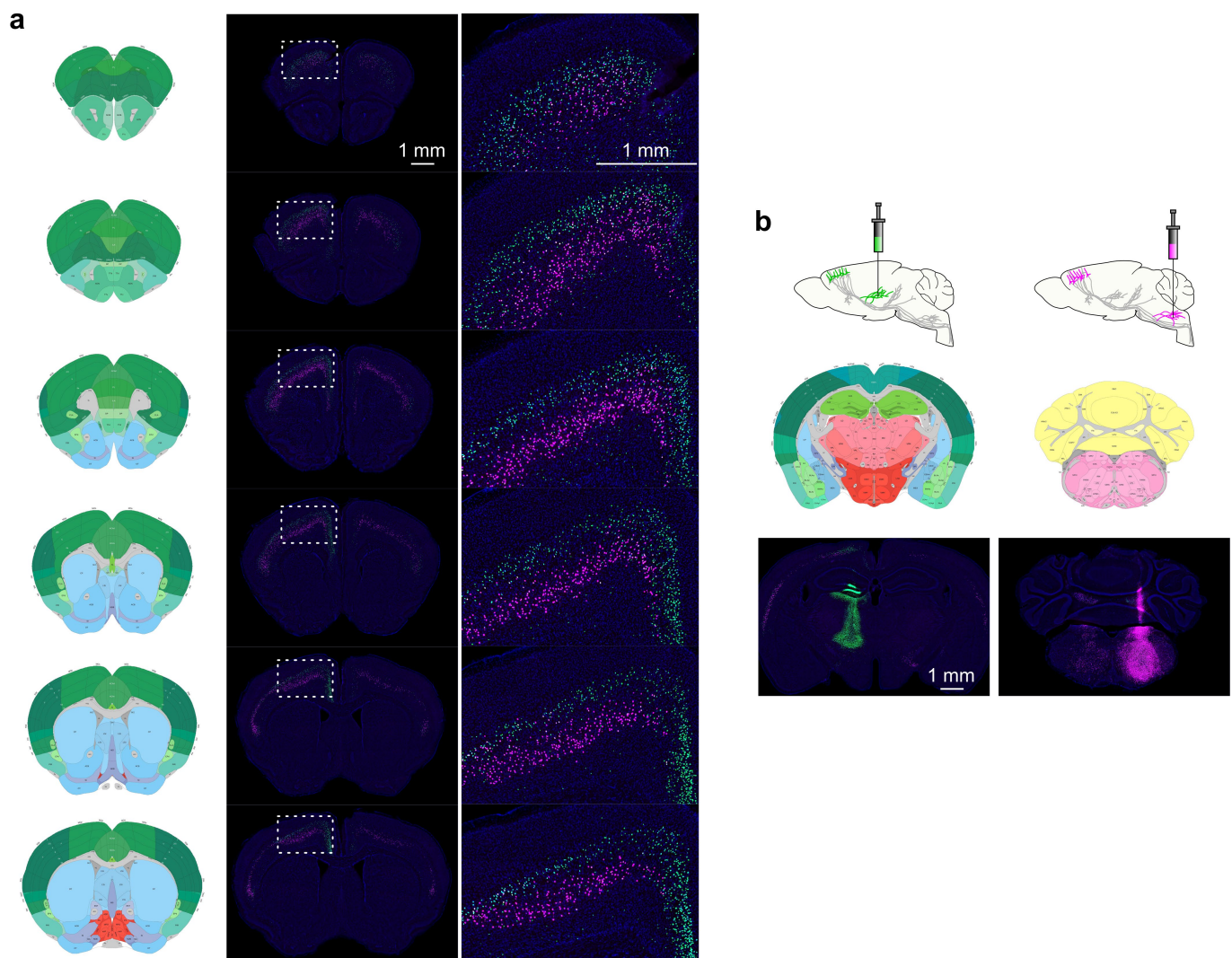
**Extended Data Fig. 1 | Differentially expressed genes in single-cell and bulk RNA-seq.** **a, b,** Heat map of expression (from scRNA-seq) of differentially expressed genes identified from scRNA-seq (**a**) and bulk RNA-seq (**b**). Columns represent individual cells, grouped by transcriptomic cluster (indicated below each colour map; *Slco2a1*,  $n = 203$ ; *Npsr1*,  $n = 43$ ; *Hpgd*,  $n = 122$ ) and retrograde labelling site (indicated above). Grey indicates cells isolated from transgenic lines or other targets. Rows represent genes differentially expressed between the *Slco2a1* and *Hpgd-Npsr1* clusters. Colour bar shows transcript expression in counts

per million mapped reads (CPM + 1) on a log-scale. **c, d,** Heat map of expression (based on bulk RNA-seq) of differentially expressed genes identified from scRNA-seq (**c**) and bulk RNA-seq (**d**) datasets. Rows represent genes, coloured by differential bulk RNA-seq expression between thalamus-labelled and medulla-labelled PT neurons. Columns in the heat map represent individual replicates (six each for  $\text{PT}_{\text{upper}}$  and  $\text{PT}_{\text{lower}}$ ). Colours show log-transformed transcript intensity (CPM + 1) in z-scored units. Blue shows replicates with low expression ( $z\text{-score} = -2$ ); red shows replicates with high expression ( $z\text{-score} = +2$ ).



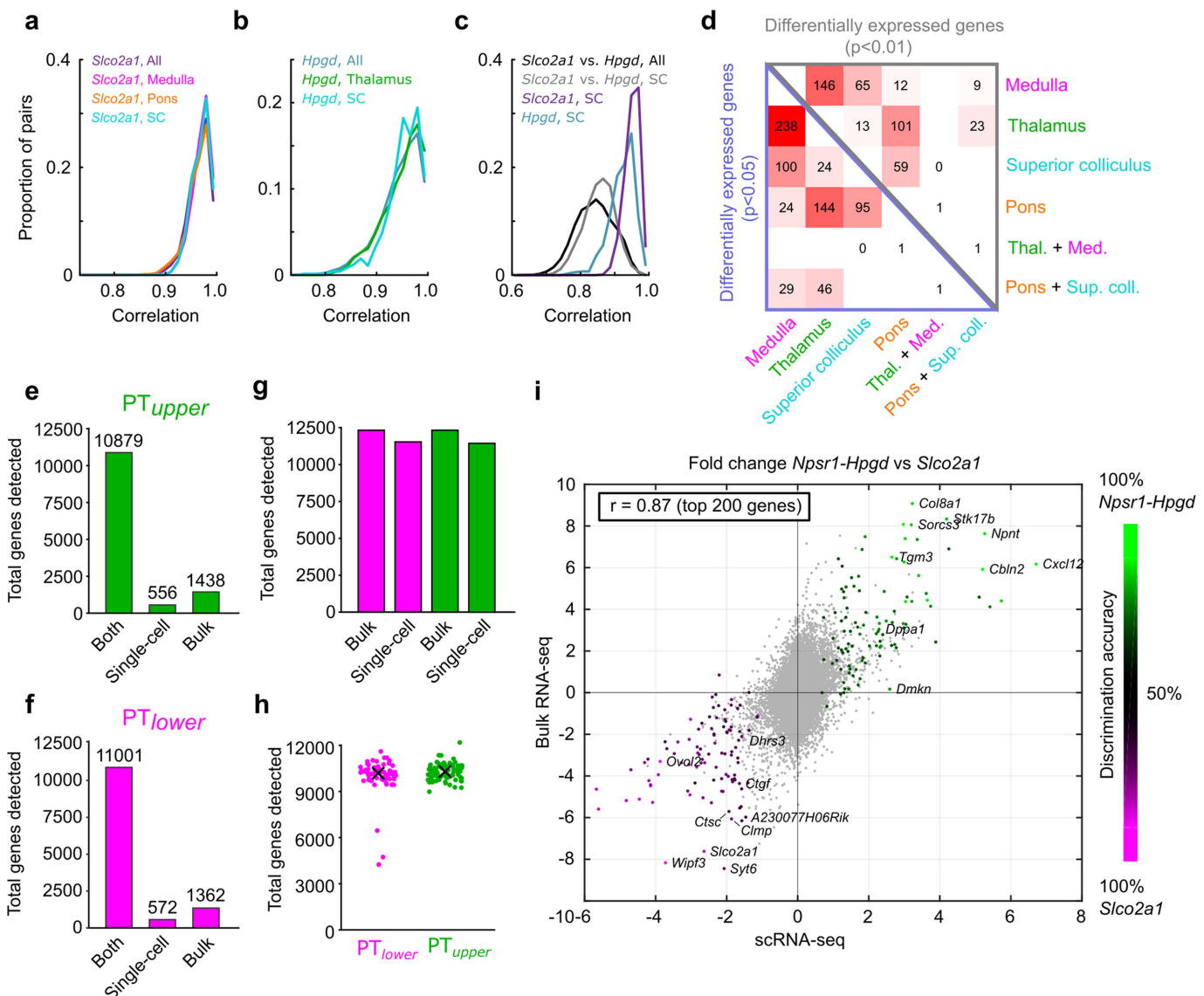
**Extended Data Fig. 2 | Distribution of PT axon collaterals.** **a**, Axonal lengths of single-neuron reconstructions within targets in thalamus and medulla (thalamus-targeting PT neurons,  $n = 8$ , green; medulla-targeting PT neurons,  $n = 4$ , magenta). **b**, Axonal lengths within other selected PT targets. **c**, Axonal termini in single-neuron reconstructions within thalamic and medullary targets. **d**, Axonal termini within other selected PT targets. **e**, Bulk projections of  $\text{PT}_{\text{upper}}$  and  $\text{PT}_{\text{lower}}$  populations. Groups of cortical neurons were labelled from the thalamus ( $\text{PT}_{\text{upper}}$ ; mouse #1), the medulla ( $\text{PT}_{\text{lower}}$ ; mouse #2), or both targets (mouse #3) using rAAV2-retro expressing spectrally distinct fluorescent proteins. Top, schematics of the labelling procedures. Left, rostro-caudal level (relative to Bregma). Right, annotated coronal sections taken from the Allen Mouse Brain Atlas<sup>54</sup> with imaged area indicated. Both cell types extended axon collaterals to motor-related superior colliculus, but to different parts. Axons from  $\text{PT}_{\text{upper}}$  cells were apparent throughout all superior colliculus layers, with a dense projection to the ventrolateral aspect;  $\text{PT}_{\text{lower}}$  neurons

were restricted to the ventral superior colliculus and were concentrated more caudally. Both groups project to the pons, particularly the pontine grey, but with terminations in largely non-overlapping zones.  $\text{PT}_{\text{upper}}$  cells projected to the globus pallidus external segment and broadly targeted the dorsal, lateral and ventral striatum.  $\text{PT}_{\text{lower}}$  cells projected sparsely to the lateral striatum.  $\text{PT}_{\text{lower}}$  neurons projected to the central amygdala and parsubthalamic nucleus.  $\text{PT}_{\text{lower}}$  neurons also made up most of the projection to the red nucleus, parabrachial nucleus, substantia nigra pars compacta, motor and sensory trigeminal nuclei in the hindbrain, and through the medullary pyramids. Both cell types extended axon collaterals locally within the same sublamina as their somata, the subthalamic nucleus, zona incerta, and the midbrain reticular nucleus.  $\text{PT}_{\text{upper}}$  cells project more broadly to layer 1 in motor cortex. Mice 1 and 2 were used for electrophysiological recordings. For this reason, projections were labelled with Chr2(H134R)-YFP.



**Extended Data Fig. 3 | Spatial distribution of thalamus- and medulla-projecting PT neurons.** **a**, The nuclei of PT neurons were retrogradely labelled from the thalamus (green cells) and medulla (magenta cells) using rAAV2-retro. Thalamus-projecting PT neurons are in upper L5b throughout motor cortex, whereas medulla-projecting PT neurons are in

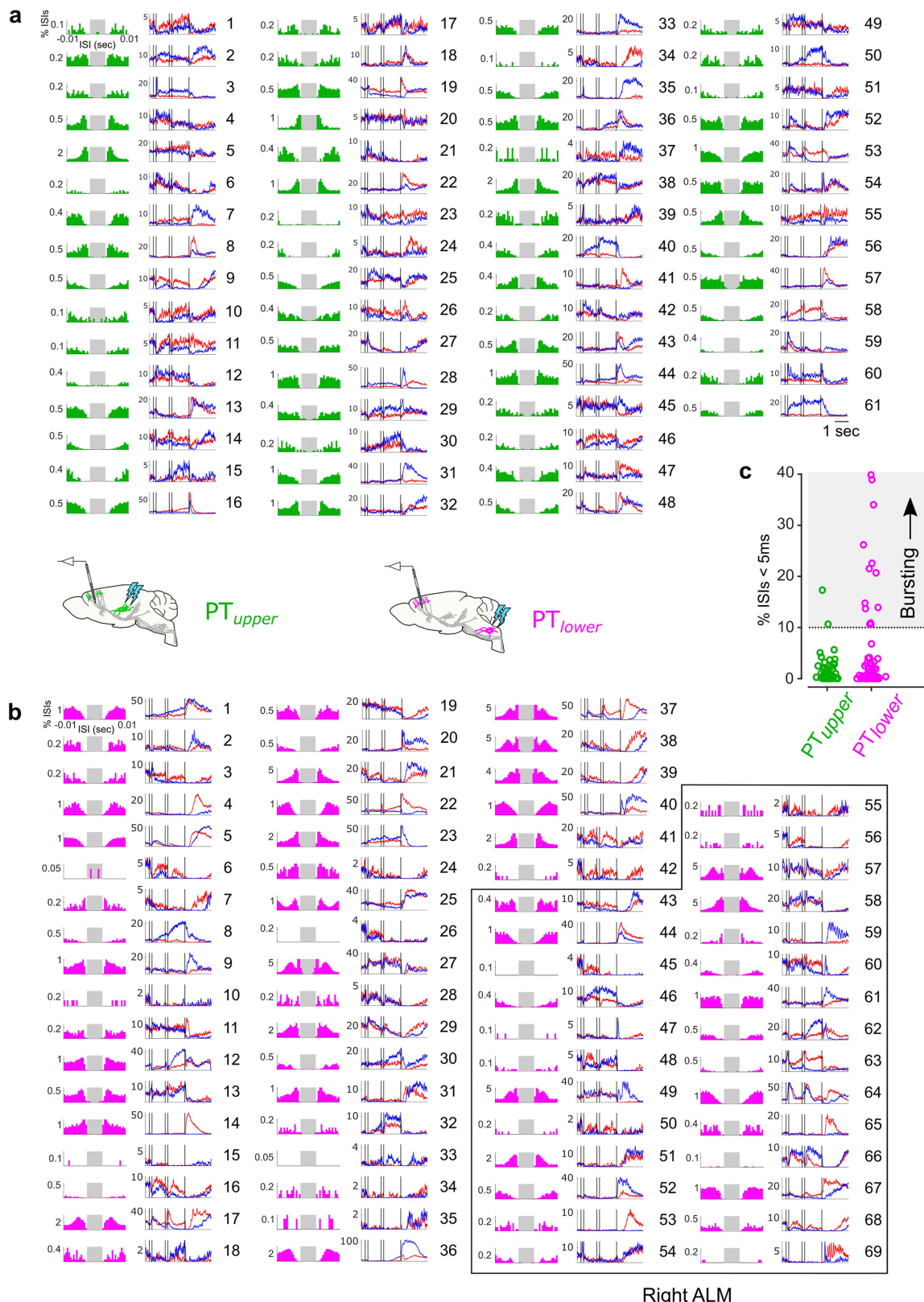
deep L5b. Schematics to the left of each image set are annotated coronal sections (Allen Mouse Brain Atlas<sup>54</sup>). **b**, rAAV2-retro injection sites in the thalamus (left) and medulla (right). Three biological replicates of this experiment yielded similar results.



**Extended Data Fig. 4 | Correspondence between scRNA-seq transcriptomic clusters, projection targets, and bulk RNA-seq data.**

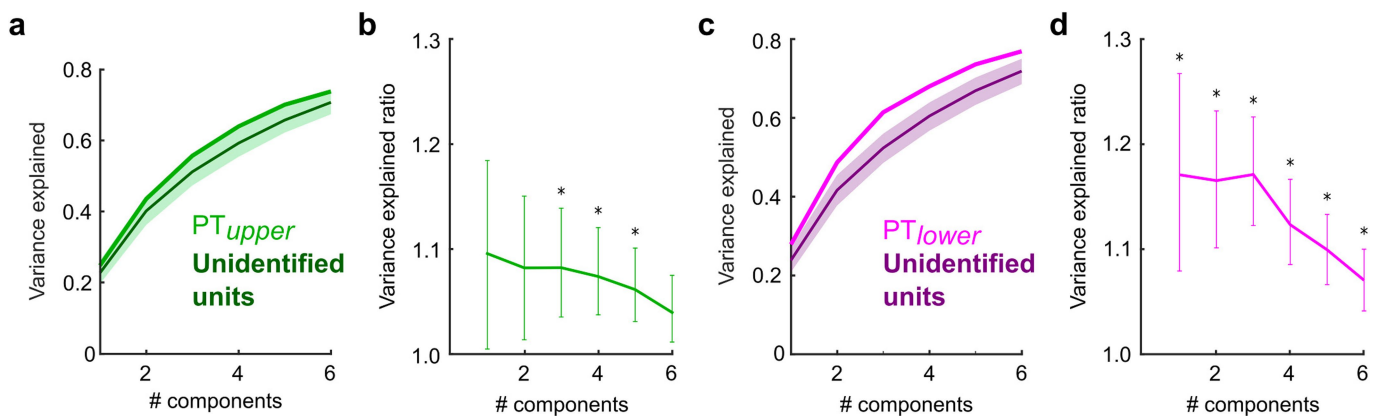
**a**, Pairwise correlations (Pearson's  $r$ ) in gene expression between all cells in the *Slco2a1* cluster and within subsets of *Slco2a1* cells identified by projection target. Expression patterns of cells identified from a common target were not more similar than randomly chosen cells. **b**, As in **a** for the *Hpgd* expression cluster. **c**, Pairwise correlation in gene expression of cells retrogradely labelled from the superior colliculus within the *Slco2a1* cluster, within the *Hpgd* cluster, and between cells from different clusters. Correlations between cells from different clusters were significantly lower than within-cluster correlations (between *Slco2a1*, superior colliculus and *Hpgd*, superior colliculus ( $n = 1,677$  pairs) versus within *Slco2a1*, superior colliculus ( $n = 903$  pairs);  $P < 1 \times 10^{-10}$ ; between *Slco2a1*, superior colliculus and *Hpgd*, superior colliculus ( $n = 1,677$  pairs) versus within *Hpgd*, superior colliculus ( $n = 741$  pairs);  $P < 1 \times 10^{-10}$ ; two-sided Wilcoxon signed rank test). Correlation analysis was not performed for the *Npsr1* cluster as the number of cells was relatively small (Fig. 2e). **d**, Number of differentially expressed genes in bulk RNA-seq data between groups of cells labelled from different projection targets. Notably, only a single gene was identified as differentially expressed between the thalamus/medulla group and the superior colliculus/pons group, indicating that the set of PT neurons projecting to either the thalamus or medulla probably represents a superset of PT neurons. There is unlikely to

be a transcriptomically distinct group of PT neurons with projections to the superior colliculus or pons that lacks projections to the medulla and thalamus. Although we cannot rule out a transcriptomically distinct subset that lacks projections to all of the thalamus, medulla, pons and superior colliculus, such neurons were not detected in single-cell reconstructions. **e**, Total genes detected by bulk RNA-seq and scRNA-seq in PT<sub>upper</sub> neurons. Both: genes detected in bulk RNA-seq and scRNA-seq; single-cell: additional genes detected only in scRNA-seq; bulk: additional genes detected only in bulk RNA-seq. **f**, As in **e** for PT<sub>lower</sub> neurons. **g**, Total number of genes detected across all experiments. In **e–g**, single cell reads were downsampled such that total read depth was the same for scRNA-seq and bulk RNA-seq. **h**, Number of genes detected in scRNA-seq for each PT<sub>upper</sub> and PT<sub>lower</sub> neuron ('X'; median; PT<sub>upper</sub>, 9,936 genes; PT<sub>lower</sub>, 9,865 genes). **i**, Mean fold change in expression (measured as  $\log_2(CPM + 1)$ ) of all genes detected by both methods between neurons in the *Npsr1-Hpgd* clusters (PT<sub>upper</sub>) and neurons in the *Slco2a1* cluster (PT<sub>lower</sub>) as determined by scRNA-seq (x axis) and bulk RNA-seq (y axis). Colour represents classification accuracy between the *Npsr1-Hpgd* and *Slco2a1* clusters using a binary (detected/not detected) version of the scRNA-seq data. The 100 most discriminative genes are coloured for each type. The correlation coefficient (Pearson's  $r$ ) in fold change expression was 0.87 for this set of 200 differentially expressed genes.



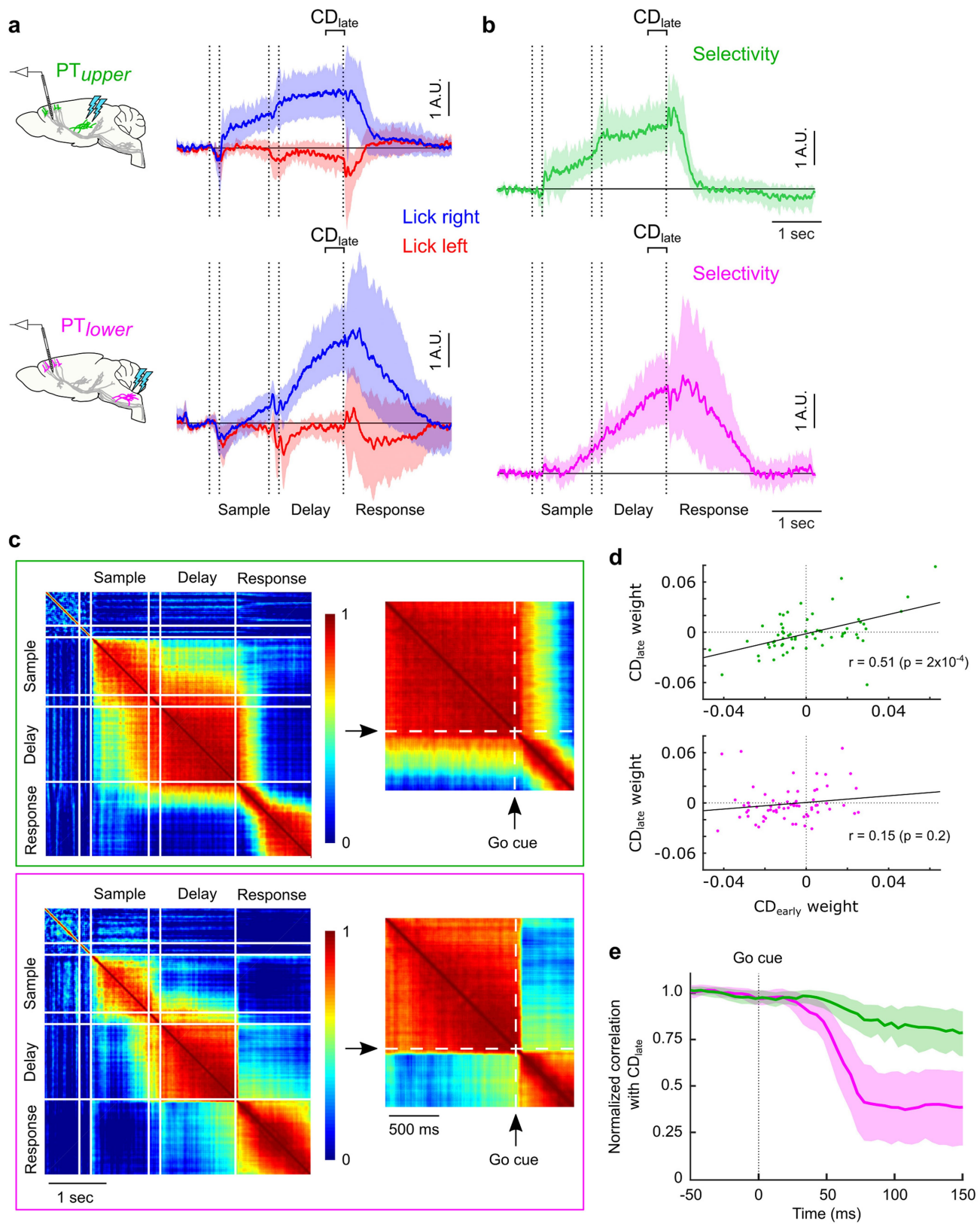
**Extended Data Fig. 5 | Electrophysiology and trial-averaged spike rates for identified PT neurons.** **a**, PT<sub>upper</sub> neurons ( $n = 61$ ). Left, inter-spike interval histograms; right: trial-averaged activity on lick right (blue) and lick left trials (red). Grey shaded area in inter-spike interval histograms represents the interval of  $-2.5$  ms to  $2.5$  ms. **b**, PT<sub>lower</sub> neurons ( $n = 69$ ). Boxed region indicates neurons recorded in the right ALM (ipsilateral to

injection site in medulla). All other neurons were recorded in the left ALM (contralateral to injection site). **c**, Bursting cells (cells in which greater than 10% of inter-spike intervals were less than 5 ms) were rare in the PT<sub>upper</sub> population (3.3%) and more common in the PT<sub>lower</sub> population (18.8%;  $P = 0.006$ , Fisher's exact test).



**Extended Data Fig. 6 | Variance in trial-averaged activity explained by PT cell class.** **a**, Green line: variance of trial-averaged activity explained by increasing numbers of principal components across the population of PT<sub>upper</sub> neurons ( $n = 61$ ). Dark green line and 95% confidence interval: expected variance explained by the same number of components for size-matched samples ( $n = 1,000$  repetitions) of simultaneously recorded,

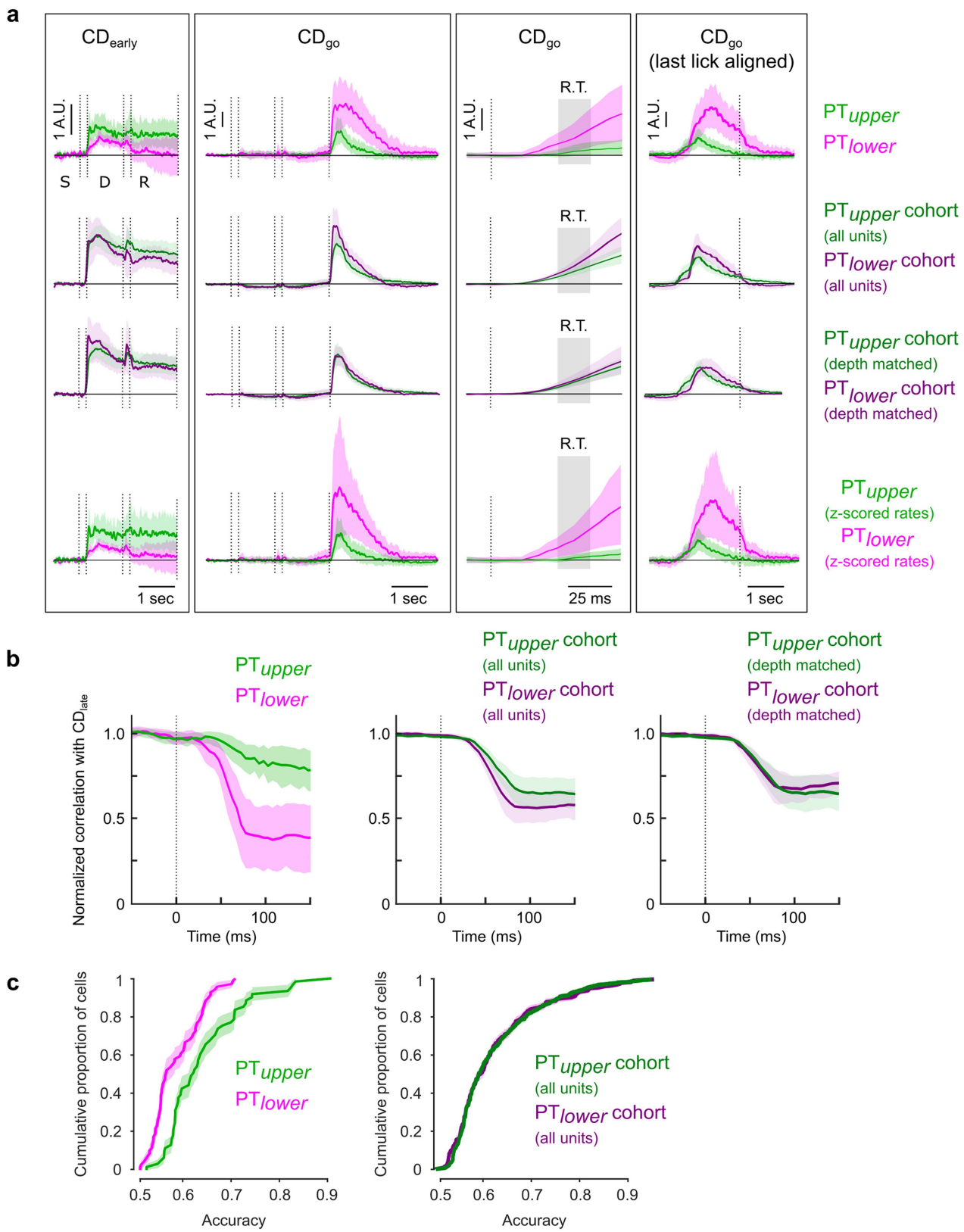
unidentified neurons. **b**, Ratio of variance explained between PT<sub>upper</sub> neurons and bootstrapped distribution of simultaneously recorded unidentified neurons. Error bars represent s.d. of distribution. **c, d**, As in **a** and **b**, but for PT<sub>lower</sub> neurons ( $n = 69$ ). Asterisks denote points significantly greater than unity ( $P < 0.05$ , bootstrap).



Extended Data Fig. 7 | See next page for caption.

**Extended Data Fig. 7 | Late delay epoch coding direction and similarity with other trial epochs.** **a**, Time course of the linear combination of neuronal activity that best differentiates trial types in the 400 ms immediately before the go cue (late coding direction;  $CD_{late}$ ) on lick right (blue) and lick left (red) trials for  $PT_{upper}$  (top;  $n = 61$ ) and  $PT_{lower}$  (bottom;  $n = 69$ ) neurons. **b**, Difference in  $CD_{late}$  projections on lick right and lick left trials (selectivity) in each population. Selectivity along  $CD_{late}$  is present in both populations, and persists after the go cue, but is not strongly modulated during movement initiation. Shaded regions represent the s.d. of the distribution produced by hierarchical bootstrapping ( $n = 1,000$  iterations) in **a** and 5–95% confidence intervals in **b** (denoting region significantly greater than zero,  $P < 0.05$  one-sided test, bootstrap). **c**, A coding direction (CD) was calculated at all individual time points. Heat maps represent the correlation (inner product) of the CD between pairs of time points. In  $PT_{upper}$  neurons (top), the coding direction remained similar across the sample and delay epochs. In  $PT_{lower}$  neurons

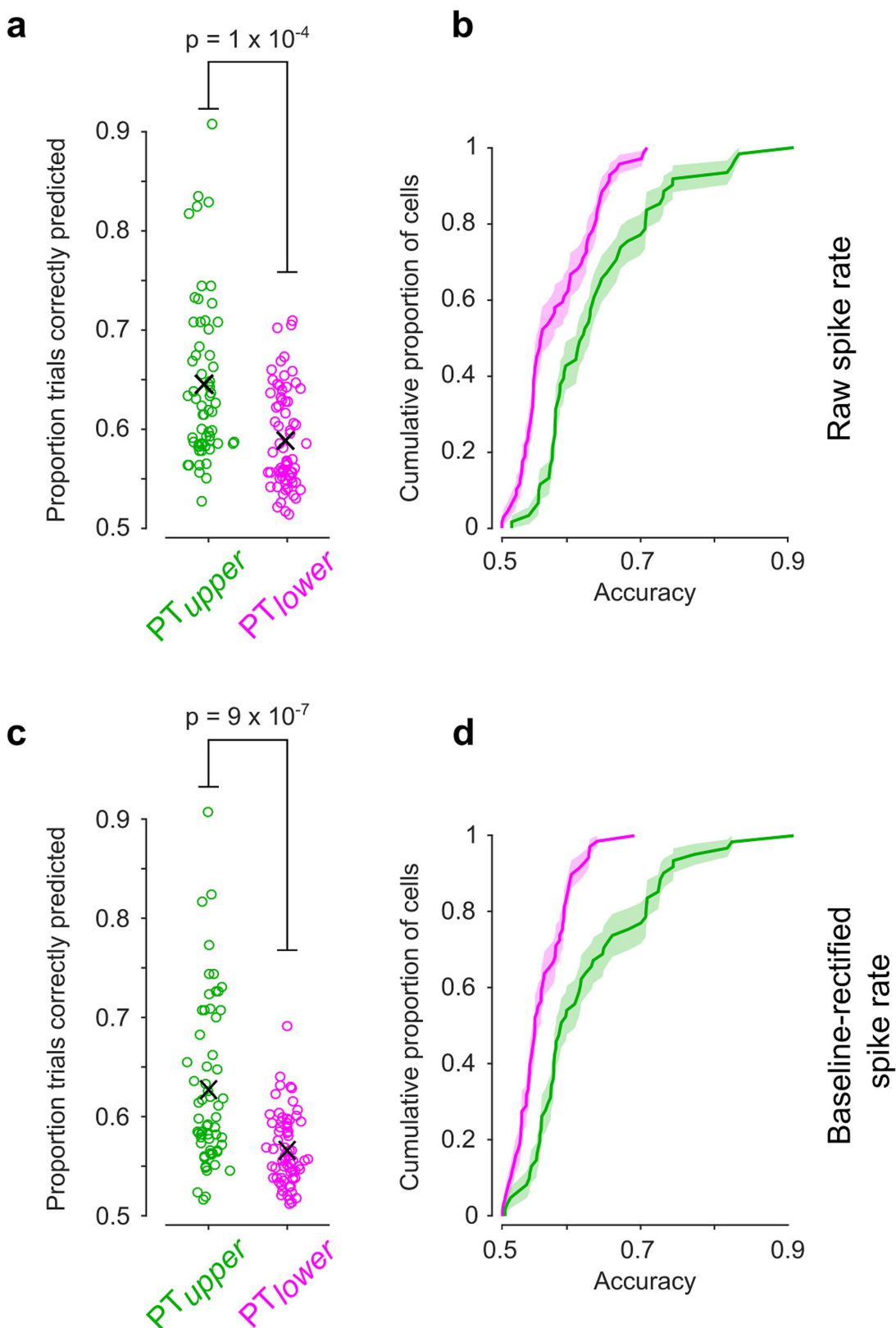
(bottom), coding directions in the delay epoch were largely orthogonal to coding directions calculated in the sample epoch. The upcoming movement direction is encoded in a persistent manner in the  $PT_{upper}$  population, but not the  $PT_{lower}$  population. Right, expanded view of the change in coding direction around the time of the go cue. An abrupt change in the coding direction occurs immediately after the go cue onset in the  $PT_{lower}$  population. A change also occurs in the  $PT_{upper}$  population, but more slowly (over several hundred milliseconds), largely after initiation of movement. **d**, Correlation (Pearson's  $r$ ) between  $CD_{early}$  vector weights and  $CD_{late}$  vector weights for  $PT_{upper}$  neurons (top) and  $PT_{lower}$  neurons (bottom). **e**, Correlation between the CD and  $CD_{late}$  normalized to the mean correlation in the 400 ms preceding the go cue. A rapid change in the CD occurs in the  $PT_{lower}$  population following the go cue. Shaded areas represent the s.d. of the bootstrapped distribution ( $n = 1,000$  iterations).



Extended Data Fig. 8 | See next page for caption.

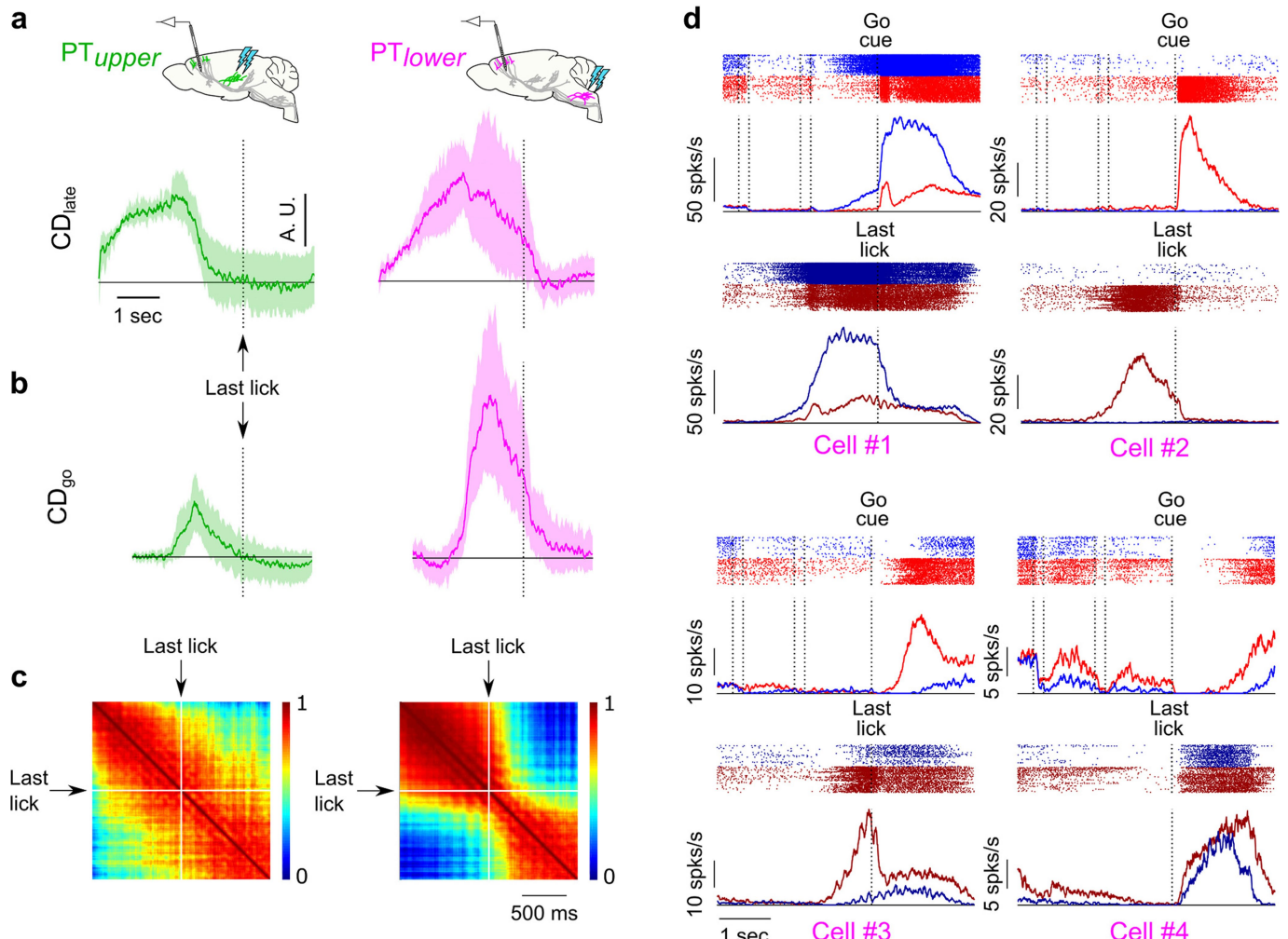
**Extended Data Fig. 8 | Comparison between identified PT populations and simultaneously recorded untagged neurons.** Time course of selectivity along CD<sub>early</sub> (as in Fig. 5b), CD<sub>go</sub> (as in Fig. 6b), and CD<sub>go</sub> aligned to the last lick in each trial (as in Extended Data Fig. 10b) calculated as follows: (1) from PT<sub>upper</sub> ( $n = 61$ ) and PT<sub>lower</sub> ( $n = 69$ ) neurons (top row), (2) from simultaneously recorded but unidentified neurons (second row;  $n = 495$  from PT<sub>upper</sub> cohort;  $n = 511$  simultaneously recorded with PT<sub>lower</sub> neurons), (3) after removing unidentified neurons from the PT<sub>lower</sub> experiments recorded from the contralateral hemisphere (third row;  $n = 276$  remaining), which were recorded at a lower average depth in a different recording configuration, and (4) from PT<sub>upper</sub> and PT<sub>lower</sub> neurons with firing rates  $z$ -scored based on their firing rates in the epoch preceding the stimulus (bottom row). CD projections in the populations of unidentified neurons were similar and nearly

indistinguishable after they were approximately depth-matched. Shaded regions represent 5–95% confidence intervals in bootstrapped distribution as in all other figures ( $n = 1,000$  iterations; denotes region significantly greater than zero,  $P < 0.05$  one-sided test, bootstrap). **b**, Correlation of CD with CD<sub>late</sub> (inner product; as in Extended Data Fig. 7e) around the time of the go cue in each PT population (left), in simultaneously recorded unidentified populations (middle) and approximately depth matched populations (right). The change in correlations around the time of the go cue in the unidentified populations were similar and intermediate between that observed in the PT<sub>upper</sub> population and PT<sub>lower</sub> populations. **c**, Early trial type decoding (as in Extended Data Fig. 9) in each PT population (left) and the simultaneously recorded populations of unidentified neurons (right).



**Extended Data Fig. 9 | Decoding of trial type in PT neuron types.**  
**a**, Accuracy of trial type classification by single neurons in the 400 ms immediately after stimulus onset. 24.6% (15 out of 61) of PT<sub>upper</sub> neurons predicted trial type with at least 70% accuracy, whereas only 4.4% (3 out of 69) of PT<sub>lower</sub> neurons did so. Mean accuracy was also significantly higher in PT<sub>upper</sub> neurons (PT<sub>upper</sub>:  $64.4 \pm 1.0\%$ ; PT<sub>lower</sub>:  $58.9 \pm 0.6\%$ , mean  $\pm$  s.e.m.;  $P = 1 \times 10^{-4}$ , two-sided Mann–Whitney test). The ten most discriminative neurons all belonged to the PT<sub>upper</sub> population.  
**b**, Cumulative distribution function of the data in **a**. **c, d**, As in **a** and **b** but decoding only based on spike rates rectified at baseline. Trial-type

selectivity during the sample epoch in PT<sub>lower</sub> neurons was predominantly characterized by a modest suppression of spiking on one trial type, probably reflecting widespread lateral inhibition. Disregarding spike rate changes below baseline, no PT<sub>lower</sub> neurons predicted trial type with at least 70% accuracy, whereas the same 24.6% of PT<sub>upper</sub> neurons continued to do so and accounted for 20 out of 21 of the most predictive neurons (PT<sub>upper</sub>:  $62.7 \pm 1.1\%$ ; PT<sub>lower</sub>:  $56.7 \pm 0.4\%$ , mean  $\pm$  s.e.m.;  $P = 9 \times 10^{-7}$ , two-sided Mann–Whitney test). As soon as the trial type is cued by the stimulus, upcoming movement direction is encoded robustly in a subset of PT<sub>upper</sub> cells and only minimally in PT<sub>lower</sub> cells.



**Extended Data Fig. 10 | Movement termination signals in PT<sub>lower</sub> neurons.** **a**, Selectivity along CD<sub>late</sub> (as in Extended Data Fig. 7b) for PT<sub>upper</sub> (green, left;  $n = 61$ ) and PT<sub>lower</sub> neurons (magenta, right;  $n = 69$ ) aligned to the last lick in the response epoch. **b**, Selectivity along CD<sub>go</sub> (same as Fig. 6b) aligned to the last lick for each PT type. Shaded regions in **a** and **b** represent 5–95% confidence intervals around the mean using hierarchical bootstrapping ( $n = 1,000$  iterations; denoting region significantly greater than zero,  $P < 0.05$  one-sided test, bootstrap). **c**, Correlation of coding direction weights at all pairs of time points after the go cue for PT<sub>upper</sub> neurons (left) and PT<sub>lower</sub> neurons (right) using

last-lick aligned spike rates. An additional transition in the population dynamics accompanies the termination of movement in PT<sub>lower</sub> neurons, whereas there is no correlate of movement termination in PT<sub>upper</sub> neurons. The change in dynamics at the offset of movement was less abrupt than at movement onset, probably a result of aligning data to the last lick-port contact, which does not precisely mark the cessation of movement. **d**, Spike raster plots (top) and trial-averaged activity (bottom) for four example PT<sub>lower</sub> neurons aligned to the go cue (lick right: blue; lick left: red) and the last lick-port contact (lick right: dark blue; lick left: dark red).

Corresponding author(s): Karel Svoboda

 Initial submission    Revised version    Final submission

## Life Sciences Reporting Summary

Nature Research wishes to improve the reproducibility of the work that we publish. This form is intended for publication with all accepted life science papers and provides structure for consistency and transparency in reporting. Every life science submission will use this form; some list items might not apply to an individual manuscript, but all fields must be completed for clarity.

For further information on the points included in this form, see [Reporting Life Sciences Research](#). For further information on Nature Research policies, including our [data availability policy](#), see [Authors & Referees](#) and the [Editorial Policy Checklist](#).

### ► Experimental design

#### 1. Sample size

Describe how sample size was determined.

For electrophysiological experiments, group sizes were based on the number of identified neurons possible to record in each animal (5-20) and the number of cells likely to yield interpretable results (> 50 neurons per condition; based on Li et al. *Nature*, 2015). For sequencing and anatomy experiments, sample sizes were similar to those used by others in the field. No statistical tests were used to determine sample sizes.

#### 2. Data exclusions

Describe any data exclusions.

Results from 2/14 animals were excluded from bulk RNA-Seq experiments (EDFigs 5,6) due to inconsistent results, as described in the methods section. During electrophysiological recordings, retrograde axonal tagging was noted to be inefficient in one mouse. This animal was excluded before spike sorting.

#### 3. Replication

Describe whether the experimental findings were reliably reproduced.

Sequencing and anatomical results were replicated across animals and across different types of experiment (sequencing: scRNAseq vs bulkRNaseq; anatomy: single cell reconstructions vs retrograde labeling). Hierarchical bootstrapping was used to estimate variability of results across animals. All presented results were reproducible across experimental replicates.

#### 4. Randomization

Describe how samples/organisms/participants were allocated into experimental groups.

In all experiments in which PT-upper and PT-lower neurons were compared in different animals (electrophysiology, *in situ* hybridization, etc.), individual mice were allocated randomly into experimental groups.

#### 5. Blinding

Describe whether the investigators were blinded to group allocation during data collection and/or analysis.

Retrogradely labeled neurons were isolated for scRNA-Seq by a technician and/or sorted automatically using FACS. Single-neuron reconstructions were performed by expert annotators without knowledge of the biological focus of this study. For electrophysiological recordings, trial types were randomly determined by a computer program. During spike sorting, experimenters did not have access to trial type, and individual events could not be related to trial epochs so experimenters were blind to conditions.

Note: all studies involving animals and/or human research participants must disclose whether blinding and randomization were used.

## 6. Statistical parameters

For all figures and tables that use statistical methods, confirm that the following items are present in relevant figure legends (or in the Methods section if additional space is needed).

n/a Confirmed

- The exact sample size (*n*) for each experimental group/condition, given as a discrete number and unit of measurement (animals, litters, cultures, etc.)
- A description of how samples were collected, noting whether measurements were taken from distinct samples or whether the same sample was measured repeatedly
- A statement indicating how many times each experiment was replicated
- The statistical test(s) used and whether they are one- or two-sided (note: only common tests should be described solely by name; more complex techniques should be described in the Methods section)
- A description of any assumptions or corrections, such as an adjustment for multiple comparisons
- The test results (e.g. *P* values) given as exact values whenever possible and with confidence intervals noted
- A clear description of statistics including central tendency (e.g. median, mean) and variation (e.g. standard deviation, interquartile range)
- Clearly defined error bars

See the web collection on [statistics for biologists](#) for further resources and guidance.

## ► Software

Policy information about [availability of computer code](#)

### 7. Software

Describe the software used to analyze the data in this study.

Matlab (2015b), JRClust (Jun et al., 2017, *BiorXiv*), R (v3.4.3), Fiji (2017-05-30; ImageJ 1.52a), STAR (v2.5.3), 3DSlicer (v4.6.2)

For manuscripts utilizing custom algorithms or software that are central to the paper but not yet described in the published literature, software must be made available to editors and reviewers upon request. We strongly encourage code deposition in a community repository (e.g. GitHub). [Nature Methods guidance for providing algorithms and software for publication](#) provides further information on this topic.

## ► Materials and reagents

Policy information about [availability of materials](#)

### 8. Materials availability

Indicate whether there are restrictions on availability of unique materials or if these materials are only available for distribution by a for-profit company.

No unique materials were used.

### 9. Antibodies

Describe the antibodies used and how they were validated for use in the system under study (i.e. assay and species).

GFP-1020 (Aves-Labs Inc.) diluted 1:100, Goat anti-Chicken AF 488 (A-11039, Invitrogen) diluted 1:100. Antibodies were used for amplification of the fluorescence of fluorescence proteins (GFP, tdTomato) and were not validated specifically for this study.

### 10. Eukaryotic cell lines

a. State the source of each eukaryotic cell line used.

No eukaryotic cell lines were used in this study.

b. Describe the method of cell line authentication used.

No eukaryotic cell lines were used in this study.

c. Report whether the cell lines were tested for mycoplasma contamination.

No eukaryotic cell lines were used in this study.

d. If any of the cell lines used are listed in the database of commonly misidentified cell lines maintained by [ICLAC](#), provide a scientific rationale for their use.

No eukaryotic cell lines were used in this study.

## ► Animals and human research participants

Policy information about [studies involving animals](#); when reporting animal research, follow the [ARRIVE guidelines](#)

### 11. Description of research animals

Provide details on animals and/or animal-derived materials used in the study.

This study is based on data from 43 mice (age > P60) of both sexes as well as additional analysis of data described in detail in a co-submitted manuscript (Tasic et al., 2017). We used wild type mice obtained from Charles River Laboratories (C57BL/6) and Jackson Laboratories (C57BL/6J) and a transgenic mouse line, EMX-IRES-Cre maintained on a C57BL/6 background. See Supplementary data tables 2 and 3 for more a complete description of the animals used for each experiment.

Policy information about [studies involving human research participants](#)

### 12. Description of human research participants

Describe the covariate-relevant population characteristics of the human research participants.

This study did not involve human research participants.